Journal of Materials Chemistry A

ROYAL SOCIETY OF CHEMISTRY

PAPER

View Article Online
View Journal | View Issue

Check for updates

Cite this: J. Mater. Chem. A, 2026, 14, 971

Atomic layer deposition of NiO_x: harnessing the potential of new precursor combinations for photoelectrochemical water oxidation

Vyshnav Kannampalli, [a] Marcel Schmickler, [bc] Bruno Fabre, [d] Ludovic Largeau, [e] Antoine Seyeux, [f] José Alvarez, [gh] Simon D. Elliott, [i] Anjana Devi [bcj] and Lionel Santinacci *[a]

This work presents the first report of thermal atomic layer deposition (ALD) of NiO_x using two nickel precursors – Alanis™ and [Ni(^{i}pki)$_2$] – in combination with two different oxygen sources (H_2O and O_3), over a temperature range of 75–250 °C. The Alanis/O_3 composition exhibited one of the highest growth rates per cycle (1.1–1.4 Å) and a broad ALD window between 100 and 200 °C. In contrast, the Alanis/H_2O and [Ni(^{i}pki)$_2$]/O_3 combinations yielded lower growth rates of 0.74 Å at 150 °C and 0.40 Å at 250 °C, respectively. Comprehensive structural, morphological, optical, and chemical characterisation revealed that the choice of precursor combination and the reaction temperature significantly impact the film composition, thereby strongly influencing its suitability for various applications. Notably, those parameters closely determined the photoelectrochemical performance and the stability of the Si/NiO_x-based photoanode towards the oxygen evolution reaction (OER). Photoelectrodes fabricated with Alanis/O_3 at 200 °C demonstrate stability exceeding 24 hours and exhibit a remarkable OER onset potential of 1.15 V *vs.* RHE for a photocurrent density of 1 mA cm^{-2}.

Received 5th June 2025
Accepted 4th November 2025

DOI: 10.1039/d5ta04555j

rsc.li/materials-a

Open Access Article. Published on 04 November 2025. Downloaded on 1/29/2026 8:32:01 PM.
This article is licensed under a Creative Commons Attribution 3.0 Unported Licence.

1 Introduction

Over the past decade, semiconductor oxides have achieved significant advancements, leading to their widespread application in various fields, including electronic devices such as photovoltaics, sensors, thin-film transistors, LEDs, and nonvolatile memory devices, as well as in catalysis, solar fuels and other emerging technologies.[1–6] Their stable electronic properties, combined with the ability to fabricate high-quality films at low temperatures,[1,6–8] make them highly attractive for diverse applications.

The studies of oxide electronics have largely focused on n-type semiconductors for both flexible and rigid devices,[2,5] but p-type oxides are gaining more and more attention due to their crucial role in next-generation technologies. These include protective and catalytic layers in photoelectrochemical (PEC) systems, transparent complementary metal-oxide semiconductors (CMOSs) for integrated circuits, hole transport layers (HTLs) in photovoltaics, and flexible p–n junctions.[9–12] Among p-type oxides, tin monoxide (SnO), cuprous oxide (Cu_2O), and nickel oxide (NiO) are currently the most extensively studied.[13] However, SnO and Cu_2O are metastable at room temperature and they tend to undergo phase transformation into n-type tin dioxide (SnO_2) or lower-band gap (E_g) cupric oxide (CuO), respectively.[5] In contrast, NiO exhibits excellent stability under ambient conditions, making it a promising candidate for various applications. For instance, in addition to its chemical and thermal stability, NiO's wide direct band gap, excellent optical transparency, and deep valence band edge (E_v) make it highly advantageous for electrocatalytic applications.

Defects are generally detrimental to many systems, particularly electronic devices. However, they can be beneficial in other fields, such as sensors or electrochemical systems for the oxygen evolution reaction (OER).[14,15] In the case of NiO, it is generally accepted that charge compensation of nickel vacancies ($V_{Ni}^{\cdot\cdot}$) is the main driving mechanism leading to p-type

[a]Aix Marseille Univ, CNRS, CINaM, Marseille, France. E-mail: lionel.santinacci@univ-amu.fr
[b]Inorganic Materials Chemistry, Faculty of Chemistry and Biochemistry, Ruhr-University Bochum, 44801 Bochum, Germany
[c]Leibniz-Institute for Solid State and Materials Research Dresden, Helmholtzstrasse 20, 01069 Dresden, Germany
[d]CNRS, ISCR (Institut des Sciences Chimiques de Rennes)-UMR6226, Univ. Rennes, Rennes F-35000, France
[e]Centre de Nanosciences et de Nanotechnologies, CNRS, Université Paris-Saclay, 91120 Palaiseau, France
[f]Institut de Recherche de Chimie Paris, Research Group Physical Chemistry of Surfaces, Chimie ParisTech-CNRS, PSL Research University, Paris 75005, France
[g]CNRS, Laboratoire de Génie Electrique et Electronique de Paris, Sorbonne Université, 75252 Paris, France
[h]CentraleSupélec, CNRS, Laboratoire de Génie Electrique et Electronique de Paris, Université Paris-Saclay, 91192 Gif-sur-Yvette, France
[i]Schrödinger GmbH, Glücksteinallee 25, 68163 Mannheim, Germany
[j]Chair of Materials Chemistry, Faculty of Chemistry and Food Chemistry, TU Dresden 01069, Germany

Open Access Article. Published on 04 November 2025. Downloaded on 1/29/2026 8:32:01 PM. This article is licensed under a Creative Commons Attribution 3.0 Unported Licence.

conductivity, since they are very easy to form as compared with oxygen vacancies.[16–19] Considering that flaws play an essential role in the properties of NiO and that it is often produced in non-stoichiometric compositions, it is referred to as NiO_x in the following. Radinger *et al.*[20] investigated the role of defects by comparing the electrochemical activity of a highly defective amorphous material with that of a single crystal. Their findings revealed that lattice defects promote the formation of $Ni(OH)_2$, facilitating its oxidation to active Ni-(oxy)hydroxides (NiOOH), which thereby significantly enhances the electrocatalytic performance.

Surface defects also have a strong influence. Weidler *et al.*[21] demonstrated that an increased surface concentration of hydroxide moieties lowers the overpotential (η) for the OER process by accelerating the $Ni(OH)_2$/NiOOH phase transition at the surface. This demonstrates the critical influence of the NiO_x surface on the expected functional properties. Moreover, it exhibits distinct surface conditions in aqueous and aprotic electrolytes, which significantly impact the OER response of the system.[22]

Since the electronic and electrochemical properties of NiO_x can be tuned by adjusting bulk and/or surface defects, it has been successfully used for water photosplitting. Recent studies have reported efficient and highly stable photoanodes by growing catalytic NiO_x layers onto silicon.[23–25] Previously, TiO_2 was deposited prior to Ni islands to protect n-Si,[26] but NiO_x is highly valuable since it acts as both a protection layer and a catalyst.

NiO_x layers can be synthesised using a wide range of techniques that potentially lead to different properties. Physical and chemical methods include pulsed laser deposition,[27] sputtering,[28] thermal evaporation,[29] sol–gel processing,[30,31] chemical bath deposition,[32] spray pyrolysis,[33] and atomic layer deposition (ALD).[34–36] The latter, in particular, offers exceptional control on a sub-nanometric scale, resulting in uniform, high-quality thin films with excellent surface coverage.[37] As a chemical method, ALD operates through a sequence of self-limited reactions, enabling the deposition of pinhole-free conformal coatings over micro- or nanostructured surfaces that can exhibit enhanced optical absorption. Such an approach has been demonstrated, for the OER, by deposition of TiO_2 on porous Si resulting in a longer electrode's lifetime and a better electrochemical response.[38] The precise control and reproducibility of ALD allow for fine-tuning of the chemical, optical, and electronic properties, ensuring consistent stoichiometry, material density, and controlled doping.[39,40] The synthesis parameters play, however, a crucial role. In previous studies, we have shown that both precursor chemistry and deposition temperature (T_{ALD}) have a critical influence on the physico-chemical and electrochemical properties on TiO_2 thin films.[41,42] In the case of NiO_x, a significant variation in lateral resistivity and electrochemical activity has recently been demonstrated in layers grown according to two different ALD processes.[43] A threefold increase in activation is reported for NiO_x grown by plasma-assisted compared to thermal ALD.

Despite the numerous benefits offered by ALD, growing NiO_x *via* this technique remains challenging. Over the past two decades, various ALD processes have been pursued to synthesize NiO_x films using different nickel and oxygen precursor combinations. These include $Ni(Cp)_2$,[44–46] $Ni(MeCp)_2$,[34,36] $Ni(EtCp)_2$,[47] $Ni(dmamp)_2$,[48] $Ni(dmamb)_2$,[49,50] $Ni(acac)_2$,[51] $Ni(apo)_2$,[52] $Ni(dmg)_2$,[52] $Ni(thd)_2$,[52] and $Ni(amd)_2$,[53] frequently paired with O_3, H_2O, H_2O_2, or O_2 plasma. However, like most metal-based ALD processes, these approaches generally result in a low growth per cycle (GPC), often less than 1.0 Å.[54–58] Recently, Holden *et al.*[59] reported ALD of NiO with a GPC of 1.2 Å using $Ni(^tBu_2DAD)_2$ with O_3 as the co-reactant. However, the requirement of a large amount of metallic precursor with a narrow ALD window further limits the usage of this precursor for wide applications.

In recent years, there has been growing interest in the development and evaluation of heteroleptic precursors for ALD. Such compounds are characterized by a metal atom bonded to two or more distinct ligands. The appeal of this approach lies in the potential to engineer a precursor that combines advantageous properties, such as enhanced vapor pressure (V_p), optimised reactivity, and improved thermal stability by integrating the desirable characteristics of the individual homoleptic parent compounds. For ALD of NiO, the heteroleptic complex $[Ni(acac)_2(TMEDA)]$ is the only reported precursor, exhibiting an impressive GPC of 2 Å, along with superior volatility and thermal stability compared to $Ni(acac)_2$.[54] However, its bulky ligands necessitate a higher Ni precursor dose to reach saturation, potentially limiting reaction kinetics. Despite promising material properties, the NiO with a large T_{ALD} range starting at a relatively low temperature (T_{ALD} < 150 °C) is still challenging due to various factors such as lower GPC, poor reaction kinetics or even the poor reactivity of the co-reactant.[49,60,61]

In this work, we report for the first time the use of two precursors in thermal ALD processes—Alanis™ (Fig. 1a), a nickel heteroleptic amidinate, and bis(4-(isopropylamino)-pent-3-en-2-onato)nickel(II), $[Ni(^ipki)_2]$, a β-ketoiminate complex (Fig. 1b). This precursor has previously been employed in both chemical vapour deposition (CVD)[62] and spatial-ALD.[63] In Alanis, R and R_1 represent CH groups restricted to alkyl chains, while R_2 refers to a substituent consisting solely of C and H atoms. Such compounds form relatively weak Ni–C bonds that are O_3 and H_2O-sensitive. Alanis shows a significantly higher vapor pressure and lower temperature stability (see the thermogravimetric analysis in Fig. S1a) with a tunable reactivity due to its heteroleptic ligand moieties, which further helps optimise the ALD process carried out at lower temperatures. On the other hand, β-ketominates are the interesting complexes having two different types of atoms (N and O)

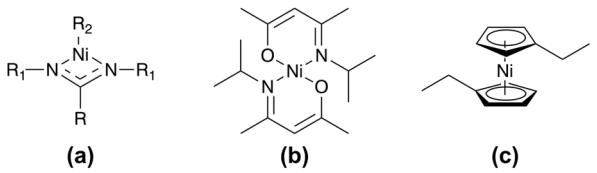

Fig. 1 Chemical formula of the Ni precursors: (a) Alanis™ (with R, R_1 and R_2 standing for hydrocarbon ligands consisting of only C and H), (b) $[Ni(^ipki)_2]$ and (c) $[Ni(EtCp)_2]$.

 This journal is © The Royal Society of Chemistry 2026

Open Access Article. Published on 04 November 2025. Downloaded on 1/29/2026 8:32:01 PM. This article is licensed under a Creative Commons Attribution 3.0 Unported Licence.

bonded to the central metal atom with tunable reactivity and stability[64] (Fig. S2).

In addition, to investigate the effect of the Ni precursors on NiO_x deposition, the influence of two co-reactants, O_3 and H_2O, is studied because they can induce different properties in the grown layers. Water proceeds *via* deprotonation, but its reactivity is limited by the steric effects of the Ni precursor and is less favourable at lower reactor temperature (T_{ALD}), resulting in slower or incomplete reactions. Using higher T_{ALD} might cause precursor desorption (limiting the growth) or thermal decomposition (resulting in CVD and poor film quality). Water adsorbs strongly, elongating the purge step, and might induce the incorporation of hydroxyl into the layer, resulting in low-quality material. However, water is an easy-to-handle, harmless compound that exhibits high vapour pressure. Conversely, O_3 is toxic but much more reactive. It may even damage the surface, introduce defects, and result in a rough deposit. A stable O_3 concentration is always required for the continuous run of ALD cycles, and high T_{ALD} can lower the O_3/O_2 ratio. It reacts with the amidinate backbone and decomposes the organic *via* a radical mechanism. In many examples, C incorporation occurs due to the formation of metal-carbonates from the reaction between O_3 and the ligands. Although O_3 might lead to a higher GPC at lower T_{ALD}, both reaction pathways exhibit detrimental effects, including ligand-fragment incorporation, stoichiometric defects, and rough layers. It is therefore difficult to predict which oxygen source is best. Consequently, it is relevant to study the process using both oxygen sources to assess their effects on the final layer properties and to select the most suitable one for the intended application.

ALD reactions are initially optimised with Alanis/O_3, Alanis/H_2O and [Ni(^{i}pki)$_2$]/O_3 precursor combinations, while [Ni(EtCp)$_2$]/O_3 (Fig. 1c), studied previously,[65] is used as a reference. A comprehensive comparative study is subsequently conducted on the morphological, structural, and chemical characteristics of the NiO_x layers, alongside their optical and photoelectrochemical properties. It is shown that the nature of the precursors and the deposition temperature drive the physicochemical and functional properties of the films.

2 Experimental

2.1 Materials

2.1.1 Sample preparation. The NiO_x deposition was performed on various substrates such as n-type silicon (Siltronix, 1–10 Ω cm, 525 ± 25 μm, single-side polished), p^+-Si (Siltronix, 0.0011–0.017 Ω cm, 255–295 μm, single-sided polished), fluorine-doped tin oxide (FTO, TEC10, from Solems), and fused-silica (FS, 150 μm, double-side polished from Neyco).

All the silicon substrates were cleaned according to the RCA cleaning protocol, consisting of initial 10 min sonications in acetone, isopropanol, and methanol, successively. The samples were then dipped in SC-1 solution for another 5 min (SC-1 is prepared by mixing H_2O, NH_3 (28%), and H_2O_2 (30%) in a volume ratio of 5 : 1 : 1 and heated at 75 °C) after rinsing thoroughly with deionized water (a resistivity of 18.2 MΩ cm). After, they were immersed, for 10 min, in SC-2 (H_2O, HCl (37%), and H_2O_2 (30%) in a volume ratio of 6 : 1 : 1, heated at 75 °C), followed by a HF (10%) dip for another 30 s to etch the SiO_2 layer. The Si wafers were rinsed with deionized water and immersed in SC-1 solution a second time. This process is repeated three times. The samples were finally rinsed with deionized water and dried under a N_2 stream. This preparation leads to a uniform SiO_2 layer with a thickness of 1–2 nm on the Si surfaces. The fused silica was cleaned using the same procedure by skipping the HF etching step. The cleaning process was performed before the deposition. The FTO substrates were cleaned initially by sonication in deionized water, followed by organic solvents such as acetone, ethanol, and isopropanol, and the substrate is kept in the isopropanol solution and taken out just before the ALD reaction.

2.2 ALD of NiO_x

NiO_x films were grown by thermal ALD in a shower-head hot-wall reactor Fiji 200 (Veeco/Cambridge Nanotech) equipped with a 10 g h^{-1} solid state O_3 generator (Plasma Technology Inc., USA) and an *in situ* M2000V spectroscopic ellipsometer (J. A. Woollam Inc) for monitoring the growth in real time. The Tauc–Lorentz oscillator model, reported earlier,[65,66] was used in CompleteEASE software (v4.72) for extracting both layer thickness (t_{NiO}) and the refractive index (n).

As mentioned above, the deposition was performed using three different Ni precursors: [Ni(EtCp)$_2$] (98% from Strem Chemicals), Alanis™ (98.4% from Air Liquide Advanced Materials[67]) and [Ni(^{i}pki)$_2$] synthesised according to a previously reported study.[62] Two O-sources were used with Alanis: O_3 and H_2O. The first one was produced from O_2 (99.999%, Linde Electronics) leading to an O_3 concentration of around 150 mg L^{-1}. Freshly produced deionized water was stored in a canister at room temperature in the second case. Ar (99.999%, Linde Electronics) served as the vector gas.

During the processes, T_{ALD} was varied from 75 to 250 °C. Its influence on the deposition is described below in Section 3. The temperature of the canister (T_c) containing the Ni precursors was adjusted to optimise V_p. Fig. S3 shows the evolution of the chamber's pressure against time. The pressure increase (ΔP) corresponding to the precursor pulse is assessed while T_c is stepped for Alanis and [Ni(^{i}pki)$_2$] and compared to [Ni(EtCp)$_2$]. T_c was set accordingly to 80, 150 and 90 °C for Alanis and [Ni(^{i}pki)$_2$] and [Ni(EtCp)$_2$], respectively, to deliver a sufficient number of molecules into the reactor (*i.e.* ΔP in the range of 0.01 torr).

The ALD cycle consisted of sequential pulse, exposure and purge steps of the Ni precursor and O source, successively. The exposure step was implemented to achieve uniform deposits and to be compatible with three-dimensional substrates. The reaction recipes of the [Ni(EtCp)$_2$] and O_3 combinations are reported earlier.[65,68] The ALD sequences for the new precursor combinations have been optimised within the present work and are reported hereinafter in Section 3. The thickness of the films was then tuned by adjusting the number of cycles (N_{ALD}).

2.3 Characterisation methods

2.3.1 Morphology and thickness of the films. The morphology of the NiO_x layers was studied by transmission

Open Access Article. Published on 04 November 2025. Downloaded on 1/29/2026 8:32:01 PM. This article is licensed under a Creative Commons Attribution 3.0 Unported Licence.

electron microscopy (TEM) using a Titan Themis 200 (Thermo Fisher Scientific). TEM lamellae were fabricated by focussed ion beam (FIB) micro-machining using a SCIOS FIB-SEM dual beam (Thermo Fisher Scientific). Chemical imaging was performed by energy dispersive spectroscopy (EDS) using a SuperX 4-quadrant (Bruker) mounted on a TEM.

In addition to ellipsometry, the thickness was confirmed by X-ray reflectivity (XRR) using an X'Pert Pro MPD diffractometer (Malvern PANalytical Inc). The incident radiation was Cu K_α (λ = 0.15418 nm) and the operating power was 45 kV and 35 mA. For the incident beam, (1/32°) and (1/16°) slits were used as divergence and cleaning slits, and a 5 mm mask was used for the lateral size of the beam. For the detection beam, a PPC (parallel plate collimator) with a 0.18° slit was used. A 0.1 mm Cu attenuator was used to measure the data until 1° in 2θ, in order to avoid the saturation of the detector. Data were fitted using GenX software (v3.7) to extract the film thickness, density and roughness.

Non-contact atomic force microscopy (AFM) was also used to measure the film roughness using an XE-100 microscope (PSIA). Root mean square roughness (R_{rms}) was determined using Gwyddion software (v2.63).

2.3.2 Crystalline structure. The crystalline structure of the NiO_x layers was determined by X-ray diffraction (XRD) using a high brilliance rotating anode (Rigaku, RU-200BH) equipped with a Fox3D Cu 12_INF mirror (Xenocs) and an image plate detector (Rayonix, Mar345). The radiation used was Cu K_α, and the beam size was 0.5 × 0.5 mm^2. The experimental resolution was about 0.3° in 2θ. In addition, selected area diffraction (SAED) was carried out using the TEM to confirm the crystalline nature of the material.

2.3.3 Chemical composition. As mentioned in Section 2.3.1, EDS was used to carry out cross sectional chemical mapping during TEM observations. X-ray photoelectron spectroscopy (XPS) was also performed at various incident angles using a NEXSA G2 (Thermo Fisher Scientific) equipped with a monochromatic Al K_α source (1486.6 eV). The take-off angle (TOA) was varied from 30 to 90° to probe either the top surface or deeper within the film, respectively. The binding energy (BE) was corrected using the C 1s peak at 284.8 eV as an internal standard. Data processing was performed with CasaXPS analysis software (v2.3.26) using a Shirley-type background subtraction. The component peaks are defined by their E_{BE}, full width at half maximum (FWHM) and Gaussian–Lorentzian envelope ratio.

The composition of the films was determined by Rutherford backscattering spectrometry (RBS) in combination with nuclear reaction analysis (NRA) experiments performed at the 4 MV accelerator facility of RUBION/Ruhr-University Bochum. RBS measurements were performed with a $4He^+$ ion beam of 2.0 MeV. With high sensitivity to O, C, and N, NRA was performed using a 1.0 MeV deuteron ion beam. The SIMNRA program was used for the processing and analysis of RBS and NRA raw data.

Depth profiling was performed by time-of-flight secondary ion mass spectrometry (ToF-SIMS) using a TOF-SIMS 5 spectrometer (IonToF GmbH, Germany) operated at a pressure of 10^{-9} mbar. Analyses were performed by applying a 2 keV Cs^+ sputter beam over a 500 × 500 μm^2 area with 100 nA target current. It was interlaced with analyses performed using a pulsed 25 keV Bi^+ primary ion source, delivering a current of 1.1 pA over a 100 × 100 μm^2 area. Negative ion depth profiles were acquired.

In addition to *in vacuo* chemical analyses, surface chemistry was also assessed *via* static contact angle (SCA) measurements using an OCA 20 instrument (DataPhysics). The experiments were conducted with 9 μL of deionised water, and contact angles were determined using SCA20 software by averaging the left and right SCAs from multiple trials.

2.4 Optical investigations

In addition to the ellipsometric investigations, the optical properties of the thin films were measured using a Cary 5000 UV-Vis-NIR spectrophotometer (Agilent) connected to an external diffuse reflectance accessory (DRA) system consisting of a ∅150 mm integrating sphere. To probe the bulk absorption of the material, 50 nm-thick films were grown on the fused silica substrates, which were used as a baseline for the measurements.

2.5 Electronic properties

The work function (W_f) of the NiO_x layers was measured with a Kelvin probe using a KP020 system (KP Technology) equipped with a ∅2 mm tungsten probe and a freshly exfoliated graphite sample as the reference. The experiments were conducted in a controlled humidity atmosphere (40%).

2.6 Electrochemical investigations

Electrochemical and photoelectrochemical investigations were carried out in a three-electrode configuration. The sample was used as a working electrode. Contact was established at the rear by placing it on a copper plate. Ohmic contact was achieved by smearing InGa eutectic on the backside of silicon. A Pt wire and a mercury/mercuric oxide electrode (Hg/HgO, 1 M KOH, E° = 0.098 V *vs.* SHE) respectively, served as counter and reference electrodes. All potentials in the following are referenced to the reversible hydrogen electrode (RHE) to account for *p*H effects. The samples were pressed against the O-ring of the electrochemical cell, leaving an area of 0.28 cm^2 exposed to deoxygenated electrolyte (N_2 bubbling) containing 1 M KOH (Sigma-Aldrich, analytical grade). The electrochemical cell was connected to an SP-200 potentiostat (Biologic SAS), and the setup was placed in a dark room to avoid any uncontrolled photoelectrochemical effects. Photoelectrochemical investigations were performed using a HAL-320 solar simulator (Asahi Spectra). AM1.5G illumination was directed onto the sample through a transparent quartz window.

The Mott–Schottky (MS) experiments are carried out in the dark, in a three-electrode configuration with a Pt wire as a counter electrode and a silver/silver chloride reference electrode (Ag/AgCl, 3 M KCl, E° = 0.212 V *vs.* SHE). Capacitance was measured as a function of applied voltage in the depletion region. A 10 mV-amplitude sinusoidal potential perturbation at a frequency (f) in the range of 12 kHz was overlaid on the DC bias. All the analyses were carried out in a monobasic phosphate buffer prepared from

 This journal is © The Royal Society of Chemistry 2026

Open Access Article. Published on 04 November 2025. Downloaded on 1/29/2026 8:32:01 PM.
This article is licensed under a Creative Commons Attribution 3.0 Unported Licence.

an aqueous solution of 1 M Na_2SO_4 and 0.1 M NaH_2PO_4. The pH of this buffer was adjusted to 11.96 by adding 1 M NaOH dropwise.

3 Results and discussion

3.1 Optimisation of the ALD processes

As mentioned above, Alanis exhibits interesting properties since it allows for depositing at relatively low temperature. Optimisation of ALD processes using this heteroleptic precursor in combination with O_3 and H_2O is compared to [Ni(^{i}pki)$_2$], a stable β-ketoiminate. The [Ni(CpEt)$_2$]-based process has been studied previously,[65,68] and it is taken as a reference (the optimised recipe and GPC are indicated in Table 1).

3.1.1 Alanis/O_3. The ALD sequence for the Alanis/O_3 combination is based on the process using Ni(EtCp)$_2$/O_3, which was optimised previously.[65,68] The study started, therefore, with pulse, exposure, and purge durations of 2 : 15 : 30 s and 0.4 : 12 : 33 s for Alanis and O_3, respectively. The purging steps were left long while optimising the Alanis and O_3 pulse times to to suppress their effect. As seen on GPC *vs.* pulse time curves at T_{ALD} = 150 °C (Fig. S4a and c), saturation is reached after 1.5 and 0.3 s for Alanis and O_3, respectively. For shorter injections, deposition does not achieve the highest GPC, while longer pulses lead to a constant value, resulting in waste of precursors.

The purge times were then assessed using these pulse times. GPCs decrease rapidly with purge time (Fig. S4b and d), reaching plateaus near 1.2 Å after 20 s. This suggests a CVD contribution for short purge times, whereas the process is self-limited after 20 s. The optimised ALD recipe is achieved with pulse, exposure, and purge sequences of 1.5 : 15 : 20 s and 0.3 : 12 : 20 s for Alanis and O_3, respectively, resulting in a GPC of 1.2 Å (see Table 1).

After such optimisation at T_{ALD} = 150 °C, saturation of the Ni precursor's pulse was assessed on the whole temperature range while keeping other parameters at maximum (see Fig. S5a). The GPC *vs.* T_{ALD} evolution could therefore be plotted with optimised sequences in Fig. 2a. It exhibits a nearly constant growth rate over a broad temperature range (100 to 175 °C) with a GPC of 1.1 to 1.2 Å. This corresponds to the so-called ALD window, where self-limited deposition occurs and thereby conformality is achieved.

At T_{ALD} = 75 °C, GPC is significantly higher (≈1.4 Å). It continuously increases with Alanis pulse time and no saturation could be observed for purge durations as long as 60 s. This behaviour can be attributed to the condensation of the Ni precursor onto the substrate. It leads to a non-self-limiting process and the composition of the film is no longer controlled (Fig. S6).

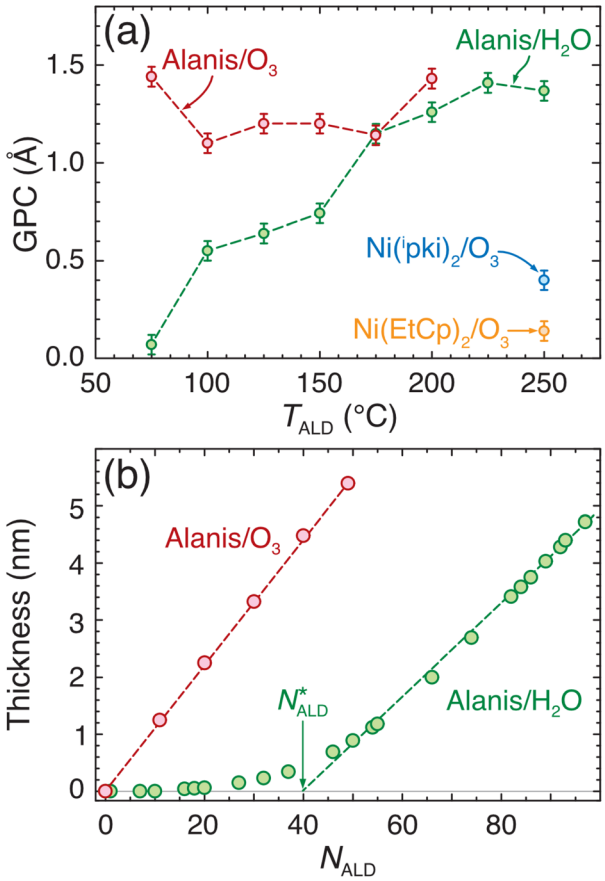

Fig. 2 The optimised ALD window of NiO_x using different precursor combinations: (a) Alanis/O_3, Alanis/H_2O, [Ni(^{i}pki)$_2$]/O_3, and [Ni(EtCp)$_2$]/O_3. (b) The evolution of the film thickness with the number of ALD cycles for Alanis/O_3 and Alanis/H_2O combinations. N^*_{ALD} is referenced in the text.

At T_{ALD} = 200 °C, GPC is also higher than the ALD window (≈1.4 Å). Such GPC improvement is usually ascribed to either precursor decomposition associated with a CVD contribution or reaction enhancement due to greater amount of energy transferred to the system. Since GPC exhibits the expected saturation trend when increasing Alanis's pulse time (Fig. S6), precursor decomposition does not seem to occur (note that Alanis's purge time was adjusted accordingly for the longest pulse time to ensure removal of physisorbed molecules). To further validate this, the ALD reaction was conducted without injecting an oxygen source. The evolution of the GPC against Alanis's pulse time (Fig. S7) indicates that no deposition occurs up to T_{ALD} = 200 °C. Weak growth is measured at higher temperatures, but it becomes significant only above 250 °C. This indicates that the

Table 1 The optimised ALD sequences for NiO_x using different precursor combinations

	Alanis/O_3	Alanis/H_2O	[Ni(^{i}pki)$_2$]/O_3	[Ni(EtCp)$_2$]/O_3
ALD sequence for the Ni precursor (s)	1.5 : 15 : 20	1.5 : 15 : 30	1.0 : 18 : 35	2.0 : 15 : 30
ALD sequence for the O source (s)	0.3 : 12 : 20	1.0 : 12 : 60	0.4 : 12 : 35	0.3 : 12 : 33
GPC (Å)	1.2	0.74	0.40	0.15
Deposition duration for 50 nm (h)	10	23	38	98

Open Access Article. Published on 04 November 2025. Downloaded on 1/29/2026 8:32:01 PM. This article is licensed under a Creative Commons Attribution 3.0 Unported Licence.

precursor is decomposing, which induces a CVD contribution to the deposition process. The latter high temperature has therefore not been considered for the Alanis/O_3 combination to avoid an uncontrolled growth process. In addition, the XRD trend indicates that the crystallinity of the as-deposited layer enhances with reaction temperature (see Fig. 4b), which further rules out the possibility of the decomposition below $T_{ALD} = 200$ °C.

3.1.2 Alanis/H_2O. H_2O is a user-friendly O-source for metal oxide synthesis *via* ALD. However, due to its lower reactivity, the metal precursor chemistry plays a crucial role in the reaction. Regarding Alanis, the high reactivity of the amidinate moiety[53,69] enables the investigation of its reaction with H_2O. Similar to the previous precursor combination, the ALD process is optimised at 150 °C by analyzing the GPC *vs.* pulse and purge time curves. According to the saturation curves (Fig. S8), the optimised sequence is then set to 1.5 : 15 : 30 s and 1 : 12 : 60 s for Alanis and H_2O, respectively, achieving a GPC of 0.74 Å. The process is then optimised within the Alanis stability temperature range, as shown in Fig. 2a. A lower GPC is observed until $T_{ALD} = 175$ °C, where it becomes close to Alanis/O_3. This lower deposition rate is in line with the lower reactivity of water compared to ozone. The H_2O-based process requires a longer purge step as water usually sticks more onto the surfaces. However, the deposition proceeds according to a self-limited reaction up to $T_{ALD} = 200$ °C (Fig. S5b). No clear ALD window can be defined, however, since GPC continuously increases up to 225 °C where thermal decomposition of the Ni precursor leads to stabilisation.

In addition to the lower GPC, a significant difference is observed between the O_3- and H_2O-based recipes. Fig. 2b compares t_{NiO} *vs.* N_{ALD} curves when using H_2O and O_3 at $T_{ALD} =$ 150 °C. In the case of O_3, a linear increase crossing the *x*-axis at 0 is observed. Conversely, for H_2O, the growth rate is initially very low ($N_{ALD} \leq 40$ cycles), and it follows the expected linear evolution only for higher numbers of cycles ($N_{ALD} \geq 40$ cycles). This retarded deposition is called nucleation delay ($N^*_{ALD} = 40$ cycles). The GPC is deduced from the slope of the linear part of the curve (*i.e.* for $N_{ALD} \geq N^*_{ALD}$). It is slightly lower than for O_3. This comparison clearly demonstrates the critical effect of the O source on the ALD of NiO. Since the difference between the two processes is the O source, the nucleation delay observed with water could be explained by its lower reactivity. Retarded nucleation can result from a different surface termination of the substrate and/or by the preferential adsorption of the liberated ligands on the substrate.[70]

Contact-angle measurements were performed to probe the surface state before ALD and after O_3 or H_2O exposures (Fig. S9). In the case of the as-prepared surfaces (RCA cleaned), an angle of 62° is measured. This low wettability reflects a low density of surface hydroxyl groups. After 30 pulses of O_3, the contact angle drops down to 32° while it remains at 63° after being exposed to 30 pulses of H_2O. This shows that the SiO_x surfaces achieved after preparation are covered with a large number of hydroxyl functions during the Alanis/O_3 process, whereas their concentration is lower for Alanis/H_2O. This might cause the nucleation delay in the latter combination.

The precursor's chemical nature also contributes. In both processes, the hydrocarbon ligand of Alanis likely reacts readily with protons on the SiO_x–OH surface and is eliminated, thereby anchoring the remaining precursor fragment to the surface, with the amidinate ligand still bound to Ni. According to literature reports,[71–73] the amidinate ligand does not detach from the Ni atom at these temperatures in the absence of a co-reactant and thus is not expected to transfer intact to the silica surface. Consequently, the observed nucleation delay unlikely results from substrate poisoning due to ligand release, as previously proposed by Goldstein *et al.*[70] The amidinate ligand might decompose so as to transfer N or NH to the silica surface, producing some form of silicon nitride (Si–N–H) that could be inert towards further adsorption, while at the same time allowing the Ni cation to extract O from Si. However, the chemical analyses of Section 3.2.2 below rule out the formation of silicon nitride, since the CN^- profiles (ToF-SIMS) are similar for both precursor combinations. Nitride formation is therefore also an unlikely reason for the nucleation delay. Decomposition of the amidinate into a carbonaceous residue (involatile C or CH_x) is another reason for the nucleation delay. H_2O might not be able to remove such a residue and it could accumulate as a H-rich carbide of silicon or of nickel (or both), resisting precursor adsorption and causing the nucleation delay. By contrast, O_3 can be expected to efficiently burn off any CH_x residue and restore the SiO_x–OH surface, ready for the next Ni pulse. The ToF-SIMS analyses in Section 3.2.2 confirm the presence of carbonaceous residue when Alanis is used in combination with O_3 and H_2O (RBS). The carbon content, however, is larger with water. ToF-SIMS profiles (Fig. 8a and b) also indicate a larger amount of C with water, with a slight accumulation at the interface. These data support the hypothesis that, while the hydrocarbon ligand of Alanis is eliminated efficiently, the amidinate ligand decomposes and coats SiO_x with an involatile carbonaceous residue that is incompletely removed by H_2O until the surface is fully covered by NiO_x (*i.e.* for $t_{NiO} \geq 4$ Å).

3.1.3 [Ni(^{i}pki)$_2$]/O_3. The excellent thermal stability of [Ni(^{i}pki)$_2$] prompted us to investigate the ALD reaction at higher temperature ($T_{ALD} = 250$ °C). The reaction is initiated with O_3 as a co-reactant, and the saturation curve is shown in Fig. S10. Since the regeneration of the vapour inside the canister is challenging for this precursor, the ALD cycle duration was increased to 100 s by slightly adjusting the exposure and purge times of the recipe. The optimised ALD recipe consists of pulse, exposure, and purge durations of 1 : 18 : 35 s and 0.4 : 12 : 35 s for [Ni(^{i}pki)$_2$]/O_3, respectively, resulting in a GPC of 0.4 Å at T_{ALD} = 250 °C (Fig. 2a). In addition to the O_3-based reactions, the process was also attempted using H_2O as the co-reactant. However, no deposition was observed under these conditions, which could be attributed to the lower reactivity of the oxygen source.

3.2 Characterization of the films

3.2.1 Morphology and crystalline structure. Fig. 3 shows TEM cross-sectional observations of NiO_x layers grown using the four precursor combinations. EDS maps (Fig. S11) confirm

 This journal is © The Royal Society of Chemistry 2026

Open Access Article. Published on 04 November 2025. Downloaded on 1/29/2026 8:32:01 PM.
This article is licensed under a Creative Commons Attribution 3.0 Unported Licence.

the chemical nature of the three areas observed on the micrographs. In all cases, NiO_x covers the Si substrate uniformly and, due to the surface preparation method, an ultra-thin SiO_x film is always present at the interface. The NiO_x thicknesses indicated in Fig. 3 are in agreement with the ellipsometric measurements and validate, therefore, the Tauc–Lorentz model.

A close observation of the NiO_x films reveals their polycrystalline structure. This is confirmed by SAED, presented in Fig. S12, where the indexed rings correspond to the main interreticular distances (d) of polycrystalline NiO_x while the spots are ascribed to the single-crystalline Si substrate.

The X-ray diffraction patterns presented in Fig. 4a are in agreement with SAED. The expected cubic rock- salt structure of NiO_x ($Fm\bar{3}m$ space group) is indeed identified. The main reflections corresponding to (111), (200), and (220) planes are, respectively, located near the expected angles of 37.279°, 43.311°, and 62.934° listed in the reference PDF card #00-047-1049. Their relative intensity is consistent with the simulated powder XRD pattern, indicating no film texturing. The lattice parameter (a), crystalline size (D), strain (ε), and dislocation density (δ) for all the films were determined from the position and full width at half maximum (FWHM) of the (200) plane and are reported in Table S1 using equations given in the SI.

All NiO_x exhibit a lattice parameter close to the expected 4.1771 Å reported in the PDF card #00-047-1049. It confirms the bunsenite-like structure of the deposited films. $[Ni(^{i}pki)_2]/O_3$ yields the best-crystallised film, as it exhibits the largest D and the lowest δ and ε. A slightly lower film quality is obtained with $[Ni(EtCp)_2]/O_3$. The Alanis-based processes exhibit smaller crystallite sizes and higher defect concentrations, as well as more strain. This could be ascribed to the high GPC observed for these precursor combinations that induces numerous nucleation sites and small crystallites. However, the nucleation delay, occurring when H_2O is used, gives rise to larger crystalline domains ($D = 11.1$ nm) than with O_3 ($D = 9.5$ nm).

Table S1 also indicates that T_{ALD} plays a significant role in the crystalline quality of the films. The largest D and lowest δ and ε are indeed measured for $[Ni(^{i}pki)_2]/O_3$ and $[Ni(EtCp)_2]/O_3$ used at 250 °C. Fig. 4b presents the evolution of the X-ray diffraction pattern for Alanis/O_3 for T_{ALD} ranging from 75 to 200 °C. At low temperature (T_{ALD} < 125 °C), the layers are amorphous while they crystallise above. As shown in the inset in Fig. 4b, the intensity of the reflection corresponding to the (200) planes increases linearly with T_{ALD}, while the FWHM simultaneously narrows. This reflects a progressive enlargement of D from 12.5 to 38.8 nm, accompanied by reductions in δ and ε from 0.6 to 0.1 × 10^{12} cm^{-2} and from 7.5 to 2.4 × 10^{-3}, respectively (for the sake of clarity, ε is plotted in Fig. S13a). It demonstrates the critical effect of T_{ALD} on the crystalline structure of the films. The effect of T_{ALD} is similar to that observed with Alanis/H_2O. Fig. S13b shows an XRD pattern of a well-crystallised film grown at $T_{ALD} = 200$ °C. However, if the temperature is increased to 250 °C, the degradation of the Ni precursor, described above, leads to poorer crystallisation because a larger amount of impurities is embedded.

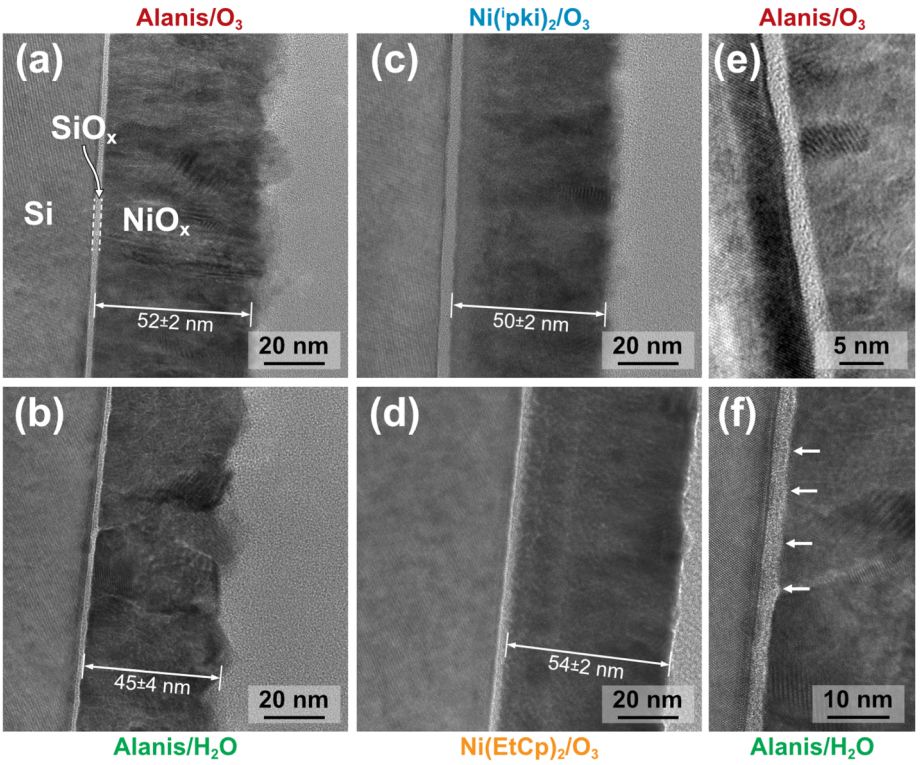

Fig. 3 TEM cross sections of NiO_x films grown using the different precursor combinations: (a) Alanis/O_3, (b) Alanis/H_2O, (c) $[Ni(^{i}pki)_2]/O_3$, and (d) $[Ni(EtCp)_2]/O_3$. (e) and (f) Are higher magnifications of the interface for Alanis/O_3 and Alanis/H_2O, respectively (arrows are referenced in the text). N_{ALD} = 450, 650, 1250, and 3600 cycles in (a), (b), (c), and (d), respectively.

Open Access Article. Published on 04 November 2025. Downloaded on 1/29/2026 8:32:01 PM.
This article is licensed under a Creative Commons Attribution 3.0 Unported Licence.

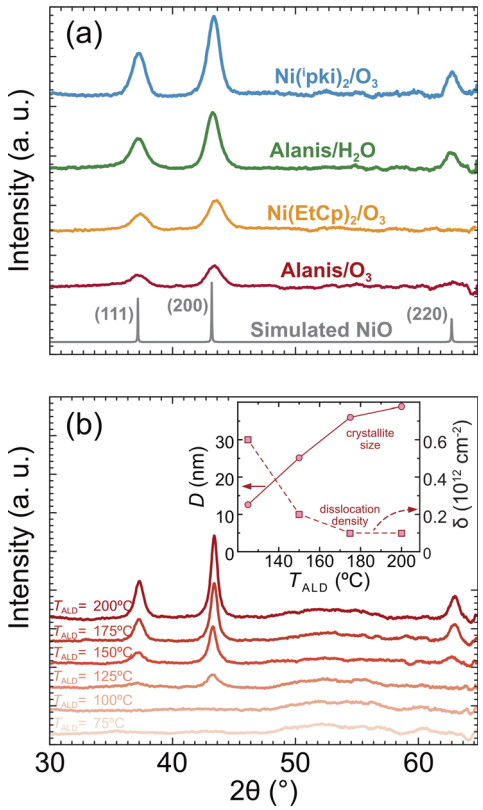

Fig. 4 (a) XRD patterns of NiO_x thin films depending on the precursor combinations (indicated on the plot). For better comparison, $t_{NiO} = 18$ nm in all cases. (b) Evolution of the XRD pattern with T_{ALD} for Alanis/O_3 (N_{ALD} has been adjusted according to each GPC to achieve $t_{NiO} = 18$ and 30 nm for (a) and (b), respectively).

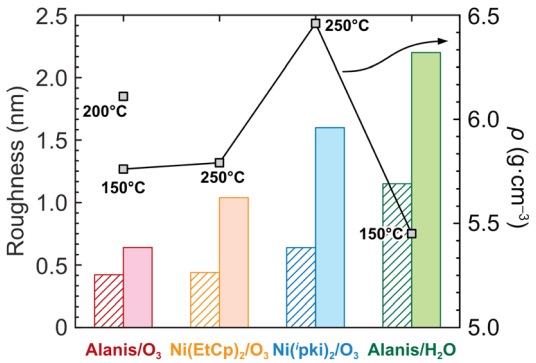

Fig. 5 Roughness of the NiO_x films measured by AFM (hatched bars) and XRR (light bars) depending on the precursor combinations: Alanis/O_3, Alanis/H_2O, [Ni(ⁱpki)$_2$]/O_3, and [Ni(EtCp)$_2$]/O_3. Grey squares correspond to the film densities depending on the precursor combinations (T_{ALD} is indicated on the plot for each value). N_{ALD} has been adjusted according to each GPC to achieve $t_{NiO} = 18$ nm.

Aside from marked grain boundaries in the case of Alanis/H_2O, Fig. 3 shows mainly that the deposited films are compact and uniform. XRR was used to assess the density of the layers (ρ) and t_{NiO}. Similarly to TEM observations, XRR data validate the ellipsometric measurements of t_{NiO} and verify, therefore, the Tauc–Lorentz model. Fig. 5 reports ρ depending on precursor recipes (raw XRR data and fittings are shown in Fig. S14). [Ni(ⁱpki)$_2$]/O_3 exhibits the highest density ($\rho = 6.46$ g cm^{-3}), which is close to the theoretical value of 6.62 g cm^{-3} for NiO. This little discrepancy is expected for polycrystalline deposits since they are disordered and usually less dense.[74] Using Alanis, the layers show a lower density. This appears to be primarily due to the reduced T_{ALD}. When NiO_x is deposited at a higher temperature ($T_{ALD} = 200$ °C), ρ increases, indeed, from 5.76 to 6.11 g cm^{-3} (Fig. 5).

In addition to ρ, XRR fitting also gives access to the roughness of the layers. These values are also plotted in Fig. 5, where they are compared to root mean square roughness (R_{rms}) extracted from AFM imaging. Such surface topography was carried out on 18 nm-thick NiO_x films grown on Si (AFM images are presented in Fig. S15).

AFM studies revealed the formation of smooth films, with roughness comparable to values reported previously.[59,75] Among the various precursor combinations, O_3-based reactions produced notably smooth films, with R_{rms} ranging from 0.42 to 0.64 nm, regardless of the precursor type or T_{ALD}, as shown in Fig. 5. Rougher surfaces are observed in the H_2O-based processes. It may result from the initial nucleation delay pointed out above that led to the larger crystallites observed in Fig. 3b. This is also why we obtain smoother films with O_3, whereas we would normally expect to see the opposite. The roughness trends are consistent with the values obtained from XRR measurements. However, the roughness values measured by AFM are lower than those derived from XRR. The root mean square roughness is generally higher than the average roughness, R_a (see the SI for definitions), and thus the discrepancy between AFM and XRR is not due to differences in roughness calculation.

Rather, it may stem from the inclusion of an additional parameter – the interface roughness between the film and the substrate. While AFM is only sensitive to the outermost surface of the film, XRR provides comprehensive information about the entire Si/SiO_x/NiO_x system. Fig. 3e and f compare the interlayer for Alanis/O_3 and Alanis/H_2O which looks rougher in the latter case (see white arrows on Fig. 3f) than for the Alanis/O_3 combination (Fig. 3e) that is the smoothest. This can again be ascribed to the nucleation delay leading to a columnar morphology when using water (Fig. 3b).

In addition to t_{NiO}, ellipsometric investigations have also given access to the refractive indices of the layers depending on the precursor combinations. Fig. 6 presents the evolution of n against λ in the visible range. In this region, n is in the range of 2 to almost 2.3 for all combinations except for [Ni(ⁱpki)$_2$]/O_3 which displays higher values (2.1 to 2.4). The current n values are lower than those reported for single-crystalline NiO.[76] This is expected since polycrystalline films are disordered and their density is lower.[74] The discrepancy between the Ni β-ketoiminate and the other compounds could, therefore, arise from the higher crystallinity observed for this precursor combination by XRD (Fig. 4a) as well as the higher density deduced from XRR. Note that the roughness does not have a significant influence on n.

This journal is © The Royal Society of Chemistry 2026

Open Access Article. Published on 04 November 2025. Downloaded on 1/29/2026 8:32:01 PM.
This article is licensed under a Creative Commons Attribution 3.0 Unported Licence.

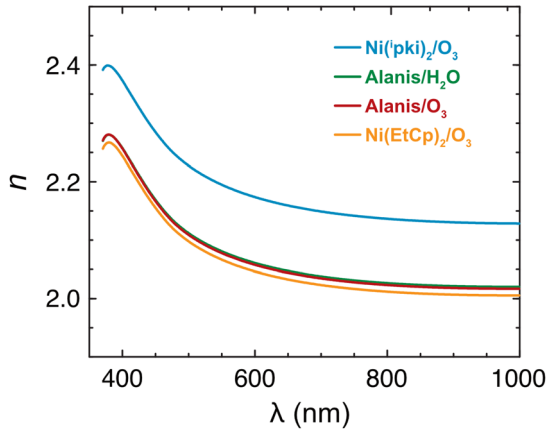

Fig. 6 Refractive index of NiO_x depending on the precursor combinations: Alanis/O_3, Alanis/H_2O, [Ni(^{i}pki)$_2$]/O_3, and [Ni(EtCp)$_2$]/O_3. N_{ALD} has been adjusted according to each GPC to achieve t_{NiO} = 18 nm.

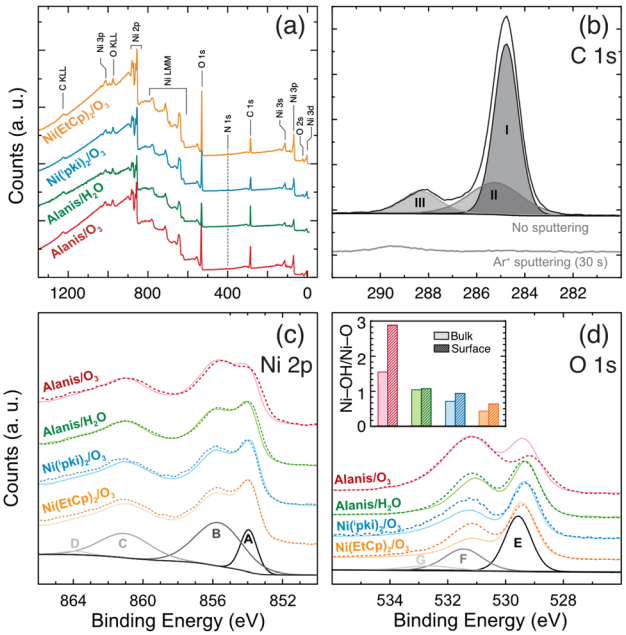

Fig. 7 XPS analysis of the NiO_x layers grown on Si depending on the precursor combinations: Alanis/O_3, Alanis/H_2O, [Ni(^{i}pki)$_2$]/O_3, and [Ni(EtCp)$_2$]/O_3. (a) Survey spectrum, (b) C 1s, (c) Ni 2p$_{3/2}$ and (d) O 1s. Full and dashed lines correspond to a TOA of 90° and 30°, respectively. Inset in (d) shows the Ni–OH/Ni–O ratios. (The Roman numbers and letters in (b–d) identify photoemission contributions referenced in the text.) N_{ALD} has been adjusted according to each GPC to achieve t_{NiO} = 18 nm.

Refractive indices are not as high as those of other polycrystalline films,[74,77] because it is known that n increases with the thickness of the films[74] or, more specifically, with the size of the crystalline domains making up the layer.[78] In the present work, the explored deposits are thin ($t_{NiO} \leq 20$ nm). This may therefore explain these lower values. It could also be due to impurities. This aspect is studied below.

3.2.2 Chemical composition. The chemical composition of the films was investigated by XPS, RBS/NRA and ToF-SIMS. XPS, in particular, is a valuable tool for understanding the chemical state of the materials. The survey spectra (Fig. 7a) indicate the presence of C, Ni, and O. When the precursor contains nitrogen (Alanis and [Ni(^{i}pki)$_2$]), a low-intensity N 1s peak is detected, indicating slight inclusion of ligands in the deposit. The substrate is not detected since there is no Si peak in the spectra. It indicates uniform surface coverage for samples analysed by XPS.

The C 1s peak is studied because it serves as a calibration and carbonaceous compounds from the precursors can be included into the films. In our system, its signal is deconvoluted into three distinct components (Fig. 7b). The primary peak at 284.8 eV corresponds to C–C bonds (Band I), while another peak at 286.4 eV is attributed to C–O species, which result from adventitious carbon contamination due to air exposure (Band II).[79] Additionally, a peak at 288.3 eV is associated with adsorbed carbonates and carbonyl groups from the ligand moieties of the precursor (Band III) as shown in Fig. 7b.[79] Notably, the C 1s peak diminished to the noise level after 30 s of Ar^+ sputtering, indicating that carbon is mainly confined to the surface and underscoring the purity of the target samples. ToF-SIMS profiling also indicates high C^- and CN^- ion concentrations at the surface that decrease quickly with sputtering time Fig. 8. In the case of [Ni(EtCp)$_2$], the carbon content remains low throughout the film, with a slight increase observed at the top surface. The CN^- ion signal is even with the background, further supporting the conclusion that the detected nitrogen in both analyses likely originates from the ligands of the nitrogen-containing precursors.

In the case of Ni, interpreting and quantifying its chemical states from the 2p doublet peak is challenging, owing to complex, extended multiplet structures, shake-up satellites, plasmon-loss features, and overlapping chemical states, all of which introduce significant uncertainty.[80,81]

The main XPS peak for Ni is the 2p$_{1/2}$ and 2p$_{3/2}$ doublet with a spin–orbit splitting (SOS) of 17.4 eV for Ni^0 and slightly larger for Ni^{2+}.[82] Curve fitting is typically performed on the Ni 2p$_{3/2}$ region in which the Ni^0 peak is expected at 853.2 eV. When the metal is oxidised, the complex line shape in the XPS spectrum primarily arises from the overlap between Ni 3d and O 2p orbitals. The primary peak, centred at 853.8 eV (Band A), is assigned to the Ni^{2+} corresponding to the Ni–O bond. A broad satellite peak at 860.9 eV (Band C) comes from the oxygen band bending effect, and a small peak at 866 eV (Band D) is attributed to the intersite charge transfer screening.[83] In addition to these peaks, there is another important shoulder peak at 855.8 eV (Band B). The origin of this peak is still debated. However, most of the literature reports attribute it to a chemical shift of Ni^{3+} species due to $V_{Ni}^{\cdot\cdot}$ and associate it with nickel hydroxides ($Ni(OH)_2$) or nickel oxyhydroxides (NiOOH) present on NiO_x surfaces.[43,80,84–86] Some reports suggest that this peak could also be related to nickel trioxide (Ni_2O_3) or result from non-local screening effects as well as surface effects.

In the present case, the SOS slightly exceeds 17.4 eV, and the characteristic Ni^0 peak at 852.3 eV is absent, indicating the expected oxidised form of Ni. Fig. 7 presents Ni 2p$_{3/2}$ depending

Open Access Article. Published on 04 November 2025. Downloaded on 1/29/2026 8:32:01 PM.
This article is licensed under a Creative Commons Attribution 3.0 Unported Licence.

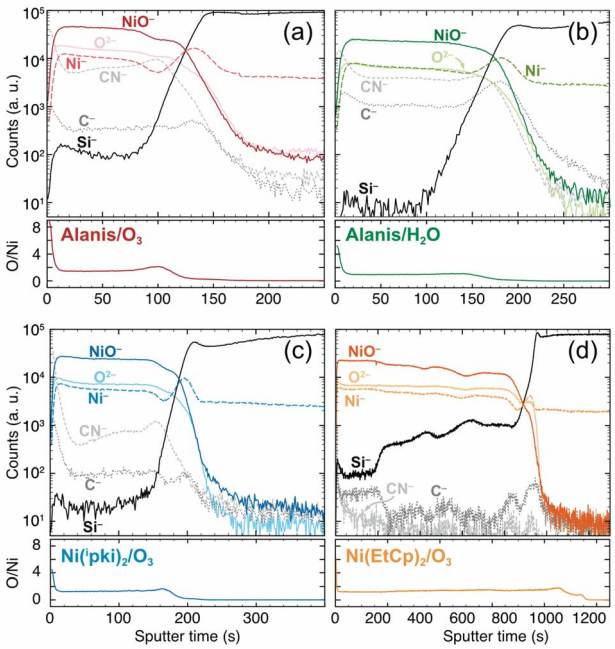

Fig. 8 ToF-SIMS profiling of NiO_x layers grown on Si depending on the precursor combinations: (a) Alanis/O_3, (b) Alanis/H_2O, (c) [Ni(^{i}pki)$_2$]/O_3, and (d) [Ni(EtCp)$_2$]/O_3. The O/Ni signal ratio is plotted below each profiling. N_{ALD} = 150, 350, 500 and 4500 cycles in (a), (b), (c), and (d), respectively.

on the precursor combinations. The low energy peak located at 854 eV corresponds to Band A, *i.e.* it originates from Ni–O bonds in NiO_x. The two peaks centered at 861.1 and 864 eV are allocated to Bands C and D, respectively. As described above, the shoulder at 855.8 eV is ascribed to Band B arising from Ni^{3+} related to Ni_2O_3, $Ni(OH)_2$ and NiOOH. Ni_2O_3 can be excluded because its signature on the O 1s peak is different from $Ni(OH)_2$. It is generally expected at 528.9 eV[87] whereas the hydroxide appears at 530.6 eV.[88] Fig. 7d shows no contribution corresponding to nickel trioxide. Furthermore, no signal of its hexagonal crystal structure is detected in XRD. This is expected because the formation of Ni_2O_3 through dehydration or dehydroxylation necessitates temperatures above 250 °C.[89] Consequently, it is difficult to clearly assign Band B to a single contribution since it could come from $Ni(OH)_2$, NiOOH, nonlocal screening effects, or surface effects without any possible distinction. It is therefore necessary to analyse the O 1s region because it provides information that can be used to discriminate between the various possibilities mentioned above.[87]

Fig. 7d presents the XPS region corresponding to O 1s for the different NiO_x films. The peak centered at 529.3 eV (Band E) confirms the octahedral bonding of Ni–O, while peaks at 531.0 eV (Band F) and 532.3 eV (Band G) are ascribed to the presence of the hydroxyl group due to either $Ni(OH)_2$ or NiOOH and H_2O.[89]

In previous studies, surface Ni–OH groups are shown to strongly influence the OER activity.[21] To study this, the evolution of Bands A and B was compared as a function of TOA that shows whether some species are more exhibited at the top surface. Although Fig. 7c indicates a slight enhancement of Band B at the top surface (TOA = 30°), dashed lines across all precursor combinations, it is challenging to draw definitive conclusions from these data, as the peak at 855.8 eV arises from multiple overlapping contributions. The Ni–OH/Ni–O ratio is therefore calculated from the O 1s region (Fig. 7d) as it decomposes into three peaks: Ni–O main peak, Ni–OH owing to the presence of $Ni(OH)_2$ and NiOOH, and the high energy component due to the adsorbed water. In all cases, the intensity of the peak at 531.2 eV is enhanced when analyses are performed at grazing incidence compared with perpendicular incidence. The Ni–OH/Ni–O ratio is thus calculated by dividing the areas of Bands E and F, respectively. It is reported in the inset of Fig. 7d for two TOA and the four precursor combinations. It shows a higher value of the Ni–OH/Ni–O ratio at TOA = 30° indicating, therefore, that the surface of the layers has a higher hydroxyl concentration than the bulk. Among the four samples, Alanis/O_3 has a significantly higher hydroxyl concentration, and its value remarkably increases on the surface (inset in Fig. 7d).

The O/Ni ratio was also investigated. It is reported in Table 2 for TOA = 30° and 90°. At normal incidence, with the exception of Alanis/O_3 for which it is close to 1.5, this ratio is very close to 1 for [Ni(EtCp)$_2$]/O_3 or slightly greater for the other combinations. This could be ascribed to $V_{Ni}^{\cdots}$. The O content is larger when the analysis is carried out using grazing incidence. This higher O/Ni ratio can be attributed to the elevated Ni–OH contribution at the surface which might be advantageous for OER activity.

Since XPS is a surface-sensitive technique, it tends to overestimate the O/Ni ratio because the surface of NiO_x becomes more oxidised when it exposed to air.[43] To gain a deeper understanding of the bulk composition of the material, XPS depth profiling was initially performed by *in situ* Ar^+ sputtering. However, in the case of NiO_x, the Ar^+ source has the ability to reduce Ni^{2+} to Ni^0,[90,91] which limits the study of the bulk composition of the film. RBS/NRA and ToF-SIMS analyses give a better view of the composition and distribution of the elements in the films.

The RBS/NRA study revealed that films based on [Ni(EtCp)$_2$]/O_3 and [Ni(^{i}pki)$_2$]/O_3 exhibit an O/Ni ratio close to unity. In contrast, films derived from Alanis/O_3 or H_2O exhibit a ratio of around 1.1 (Table 3). This is in line with the XPS quantification. It indicates that the NiO_x layers grown using [Ni(EtCp)$_2$]/O_3 and [Ni(^{i}pki)$_2$]/O_3 contain fewer defects than with Alanis. As an excess of oxygen is observed in the latter, the flaws are most likely $V_{Ni}^{\cdots}$. When T_{ALD} is increased to 200 °C for Alanis/O_3, a stoichiometric oxide is observed, indicating a lower defect

Table 2 O/Ni ratios of the NiO_x layers for the different precursor combinations calculated from AR-XPS at two TOAs (TOA = 30° and 90° correspond to grazing (top surface) and normal (bulk) incidence)

TOA	Alanis/O_3	Alanis/H_2O	[Ni(^{i}pki)$_2$]/O_3	[Ni(EtCp)$_2$]/O_3
30°	2.04	1.17	1.07	1.04
90°	1.54	1.06	1.06	0.99

This journal is © The Royal Society of Chemistry 2026

Open Access Article. Published on 04 November 2025. Downloaded on 1/29/2026 8:32:01 PM.
This article is licensed under a Creative Commons Attribution 3.0 Unported Licence.

Table 3 RBS/NRA analysis of the NiO_x films for the different precursor combinations and T_{ALD}

Prec. combinations	T_{ALD} (°C)	Ni (at%)	O (at%)	C (at%)	N (at%)	O/Ni
Alanis/O_3	150	44.99	49.85	3.56	1.60	1.11
	175	45.94	52.44	0.00	1.62	1.14
	200	48.50	48.89	1.53	1.07	1.01
Alanis/H_2O	150	42.47	48.57	7.59	1.38	1.14
[Ni(^{i}pki)$_2$]/O_3	250	47.64	49.70	2.50	0.16	1.04
[Ni(EtCp)$_2$]/O_3	250	49.96	49.53	0.51	0.00	0.99

concentration. This is in line with the increase in density (ρ = 6.1 g cm^{-3}) observed by XRR when the Alanis/O_3 process is carried out at 200 °C (Section 3.2.1).

As mentioned above, when the nickel precursor contains a nitrogen function, the film has a very low nitrogen content. Except for [Ni(EtCp)$_2$]/O_3, which appears relatively pure, the other films contain a small amount of carbon. This contamination is slightly higher for Alanis/H_2O. As mentioned above, it is likely due to the weaker water reactivity compared to ozone, resulting in less efficient ligand elimination during the process. For Alanis/O_3, increasing T_{ALD} appears to reduce contamination. Note that the zero carbon concentration observed at T_{ALD} = 175 °C is attributed to the very low thickness of the analysed film, which placed the carbon content below the detection limit.

The concentration profiles obtained by ToF-SIMS are in agreement with the results obtained by XPS and RBS/NRA. Fig. 8 presents the composition profiles for the different precursor combinations. As revealed by XPS, the high C content at the surface is ascribed to adventitious contamination. Impurity levels (C and N) in the bulk films are also consistent with the RBS/NRA results. No N is detected for [Ni(EtCp)$_2$] as it does not contain a nitrogen atom. Similarly, the C level is qualitatively higher for Alanis/H_2O than for the others because H_2O is not sufficiently reactive to remove the residues. The nitrogen detected in Alanis- and [Ni(^{i}pki)$_2$]-based processes is evenly spread over the whole NiO_x layer. The surface oxygen enrichment spotted by XPS is not easily discernible from the Ni^- and O^{2-} signals. Thus, the O/Ni ratio is plotted below each analysis. It confirms a higher oxygen concentration at the top surface while remaining constant across the rest of the film. In the case of [Ni(EtCp)$_2$]/O_3, the Si^- signal increases in steps as the analysis progresses in depth. This can be attributed to non-uniform deposition, which allows the substrate signal to appear earlier in some locations. Deposits made with Cp-based precursors are indeed less reproducible than those made with other precursors.

3.2.3 Optical properties. Since NiO_x is a p-type semiconductor, it absorbs light with energy greater than E_g. Therefore, measuring its optical properties is essential to understanding the photoconversion mechanisms at the n-Si/NiO_x/electrolyte interface. This is particularly important given that the precursor combination appears to significantly influence the film's properties, as demonstrated above. Fig. 9 presents transmittance (T), reflectance (R) and absorptance (A) depending on the wavelength of the incident beam. Note that A is calculated by subtracting R and T from 100%.

In all cases, T is greater than 60% for $\lambda \geq 375$ nm (Fig. 9a). When comparing T with R and A (Fig. 9b and c), it appears that the main optical loss arises from the reflectance since absorptance is very low. This is expected, as the material's bandgap is in the UV range. While films formed using most precursor combinations at different temperatures are highly transparent, the Alanis/O_3 combination behaves differently. In this case, an absorptance tail in the visible range is measured. This can be attributed to energy states located in the bandgap. It is further confirmed by the Tauc plot presented in Fig. 9d, where E_g is calculated according to the Tauc relation (eqn (1)) by considering a direct optical transition in NiO_x (*i.e.*, $\gamma = \frac{1}{2}$).

$$(\alpha h\nu)^{1/\gamma} = A(h\nu - E_g) \quad (1)$$

Except for Alanis/O_3 for which E_g = 3.71 eV, it is around 3.85 eV for the other precursor combinations. This is in line with the literature where values ranging from 3.1 to 4.3 eV are found[92,93] with 3.7 to 3.8 eV being the commonly accepted range.[76,94]

[Ni(^{i}pki)$_2$]/O_3-based films exhibit the highest transparency with lower absorption (Fig. 9a and c). This can be attributed to

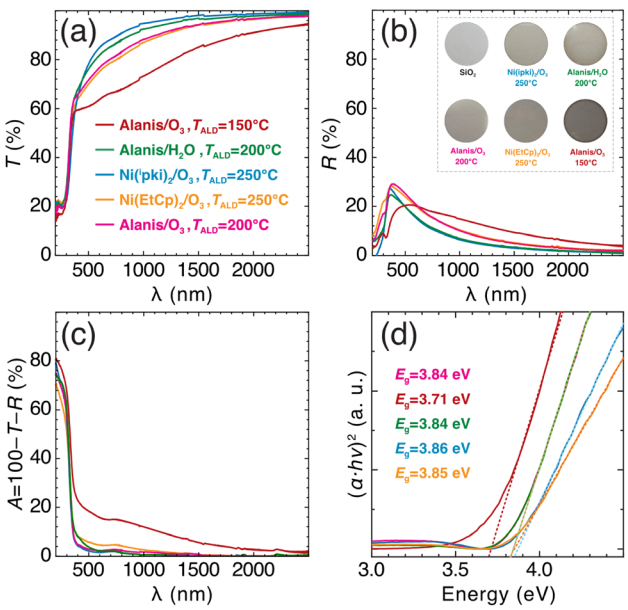

Fig. 9 UV-Vis NIR spectra: (a) transmission, (b) reflectance, (c) absorptance, and (d) Tauc plot. All the measurements are performed by using air as the baseline. The linear extrapolations (dashed lines) in (d) give the E_g values indicated on the plot. N_{ALD} has been adjusted according to each GPC to achieve t_{NiO} = 50 nm.

Open Access Article. Published on 04 November 2025. Downloaded on 1/29/2026 8:32:01 PM.
This article is licensed under a Creative Commons Attribution 3.0 Unported Licence.

their well-crystallised structure, which reduces the grain boundary surface area, as well as to their near-unity O/Ni ratio and low contamination level (Tables 2 and 3).

Temperature can also play a critical role in transparency. Annealing above 200 °C shows higher transparency by reducing defect concentration.[95] In the present work, lower T_{ALD}, which results in a higher concentration of NiOOH surface states and defects, likely contributes to the lower transmittance observed in the Alanis/O_3-based layers when they are grown at 150 °C, while they become transparent at 200 °C. The absorption tail observed for Alanis/O_3 at $T_{ALD} = 150$ °C can thus be ascribed to energy states within the bandgap. Such behaviour is commonly observed for transition-metal oxides because achieving precise stoichiometry is inherently challenging. For NiO_x, this difficulty is primarily due to the prevalence of defects, particularly $V_{Ni}^{\cdot\cdot}$, which cause E_g to vary.[94,96,97] Temperature appears to be a critical factor influencing the optical properties, as increasing T_{ALD} leads to better-crystallised films with fewer defects and impurities and an O/Ni ratio approaching unity.

3.2.4 Mott–Schottky analysis. Chemical analyses have shown that the film composition varies with the precursor combination or the deposition temperature. Among the defects mentioned, $V_{Ni}^{\cdot\cdot}$ can have a significant effect on the doping of NiO_x layers. Mott–Schottky analyses have thus been performed in monobasic phosphate buffer with a pH = 11.96 on layers grown on FTO (Fig. 10). According to eqn (2), it is possible to determine the doping and the flat band potential (U_{fb}) of the layers.

$$\frac{1}{C^2} = \frac{2}{A^2 \varepsilon \varepsilon_0 e N_a}\left(U - U_{fb} - \frac{kT}{e}\right) \quad (2)$$

where ε is the relative dielectric constant of the semiconductor ($\varepsilon_{NiO} = 12$),[98] ε_0 is the permittivity of free space, N_a is the carrier concentration (positive for holes), A is the area of the electrode, U is the applied potential, k is the Boltzmann constant, T is the temperature, and e is the unit charge.

In all cases, a linear evolution is observed in the depletion region. The negative slopes confirm the p-type behaviour of the material. NiO_x films deposited using Alanis exhibit high doping levels on the order of 10^{20} cm^{-3}, whereas those grown from the β-ketoiminate precursor are significantly less doped, with concentrations around 10^{18} cm^{-3}. This is consistent with the stoichiometric composition of the film (O/Ni = 1) when the Cp-based precursor is used. In contrast, Mott–Schottky analyses confirm that, in the other cases, the doping originates from Ni deficiency in the NiO_x matrix. A slight decrease in N_a was observed with increasing T_{ALD} for the Alanis/O_3 combination (Fig. 10d). Here again, the reduced doping is attributed to a more balanced O/Ni ratio.

As indicated by eqn (2), the x-intercept of the linear fit gives U_{fb} that ranges from 0.70 to 1.03 V *vs.* RHE depending on the ALD processes. Although these values span approximately 300 mV, they remain within the range generally reported for this material at pH = 11.96 (0.65 to 1.15 V *vs.* RHE).[36,53,99,100] Variations in U_{fb} can arise from many factors, but as previously reported in the case of NiO_x ALD, the precursors[53] and T_{ALD}[101] appear to be critical. Fig. 10 shows that the Alanis/O_3 combination at 150 °C has the lowest U_{fb} (0.70 V *vs.* RHE). XPS analyses have indicated that this precursor combination leads to a high concentration of surface hydroxyls. According to the literature,[101] this causes a negative U_{fb} shift at the NiO_x/electrolyte interface, and this is often considered to contribute to a higher OER activity. The other precursor combinations show more positive results for U_{fb} (0.93 and 1.03 V for Alanis/H_2O and [Ni(^{i}pki)$_2$]/O_3, respectively) because they have lower surface hydroxyl concentrations. In addition, NiO_x grown from Alanis/O_3 at $T_{ALD} = 200$ °C leads to a more positive U_{fb} (0.86 V). This is probably due to a lower concentration of –OH on the surface.

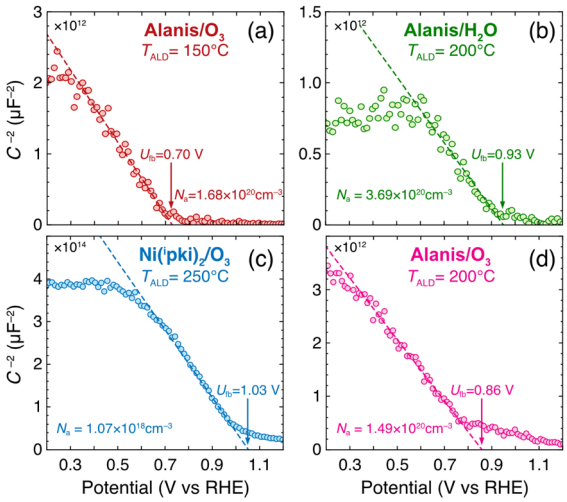

Fig. 10 Mott–Schottky plots of NiO_x layers deposited from (a) Alanis/O_3 at 150 °C, (b) Alanis/H_2O at 200 °C, (c) [Ni(^{i}pki)$_2$]/O_3 at 250 °C and (d) Alanis/O_3 at 200 °C. U_{fb} and N_a are indicated on the plots. Capacitance measurements are performed with an AC voltage of 10 mV in 1 M Na_2SO_4 + 0.1 M NaH_2PO_4 at $f = 12$ kHz. N_{ALD} has been adjusted according to each GPC to achieve $t_{NiO} = 50$ nm.

3.3 Electrochemical activity toward the OER

As mentioned in the Introduction, NiO_x layers have been proposed as protective layers and catalysts for Si-based photoanodes.[23] Section 3.2 demonstrated the significant influence of the precursor combination and deposition temperature on the physicochemical properties. In the following, the photoelectrochemical response of the anodes is investigated as a function of their synthesis parameters. The Si therefore drives the electrode/electrolyte interface.

The influence of t_{NiO} on the OER response was first studied using the Alanis/O_3 combination. Although the interface consists of a double junction, n-Si/p-NiO_x/electrolyte, potentiometry performed in the dark and under illumination (Fig. S16a) reveals a negative photopotential ($U_{ph} \approx -450$ mV). This indicates that the interface behaves like an n-type semiconductor/electrolyte junction. It is confirmed by the MS plot (Fig. S16b), which shows a linear trend with a positive slope between 1.5 and 3.0 V, indicating that Si drives the electrode/electrolyte interface. This is expected, since holes (h^+) have to be photogenerated in the Si to feed the OER, while NiO_x has to act as a catalyst and protection against corrosion.

 This journal is © The Royal Society of Chemistry 2026

Open Access Article. Published on 04 November 2025. Downloaded on 1/29/2026 8:32:01 PM.
This article is licensed under a Creative Commons Attribution 3.0 Unported Licence.

Fig. 11a shows cyclic voltammograms (CVs) recorded on layers with t_{NiO} ranging from 10 to 50 nm. As expected for such n-type Schottky junctions, CVs recorded in the dark exhibit a negligible anodic current. In contrast, under illumination, the curves display significant photocurrent (j_{ph}) with a steep increase starting around 1.05 V—corresponding to water oxidation—and a plateau ($j_{ph} \approx 27$ mA cm^{-2}) starting near 1.8 V. It is consistent with the U_{fb} of 0.7 V (Fig. S16b), which is expected at a slightly more cathodic potential than the j_{ph} initiation. While t_{NiO} does not affect the level of the current plateau, it influences the onset potential. By comparing the overpotential (η_{10}) at $j_{ph} = 10$ mA cm^{-2}, a 450 mV negative shift is measured for NiO_x layers grown on n-Si with respect to those deposited on p$^+$-Si (*i.e.* a degenerated semiconductor that is not light-sensitive). Additionally, η_{10} shifts negatively, from 1.61 to 1.41 V, as t_{NiO} increases from 10 to 20 nm, respectively, but it remains almost constant from 20 to 50 nm ($\eta_{10} = 1.42$ V). This confirms that NiO_x acts as a hole-trapping co-catalyst, facilitating water oxidation.

The thickness-dependent performance underscores the balance between catalytic activity and charge-carrier mobility in NiO_x. For layers thicker than 20 nm, one can consider that bulk properties are observed.

As predicted by the previous characterisation, the photoelectrochemical responses of NiO_x layers should vary depending on the precursor combinations. Fig. 11b compares the initial CVs recorded under AM1.5G illumination for Alanis/O_3, Alanis/H_2O, and [Ni(^{i}pki)$_2$]/O_3. The three CVs exhibit, indeed, different behaviours. The comparison of the curves indicates that the highest photoresponse is observed for films deposited from Alanis/O_3, followed by [Ni(^{i}pki)$_2$]/O_3, and finally Alanis/H_2O. The expected constant photocurrent ($j_{ph} \approx 27$ mA cm^{-2}), starting at 1.9 V, is proportional to the illumination flux. Conversely, lower currents and no plateau are observed for the other precursor combinations. The j_{ph} fluctuations that can appear on the plateau are attributed to O_2 bubbles formed during the OER. This effect is even stronger in Fig. 11d. Similarly, the values of η_{10} are 2.15, 1.78, and 1.42 V for films prepared using Alanis/H_2O, [Ni(^{i}pki)$_2$]/O_3, and Alanis/O_3, respectively. W_f values are listed in Table 4 with the E_g measured above. The combinations of precursors lead to values of W_f and E_g that are very close to each other. It is therefore difficult to explain the differences observed in Fig. 11b by a different band structure of the electrode/electrolyte junction.

This can be attributed to the higher surface hydroxyl concentration observed when using Alanis/O_3. Hydroxylation of the NiO_x surface indeed plays a critical role in the catalytic activity.[21] During cyclic polarisations, phase transformations between different hydroxides (α- and β-Ni(OH)$_2$) and oxyhydroxides (β- and γ-NiOOH) occur, which drive the OER kinetics.[20,43] The chemical analyses presented above show high O/Ni (Table 2) and high Ni–OH/Ni–O (Fig. 7d) ratios for this precursor combination. These values are lower and close for both [Ni(^{i}pki)$_2$]/O_3 and Alanis/H_2O but the latter leads to a much more contaminated layer (Table 3) that could hamper the electrochemical reaction. The surface hydroxyl concentration can also be monitored by MS analysis, as a high –OH termination density typically induces a negative shift of U_{fb}.[102] U_{fb} for Alanis/O_3 is accordingly the lowest (0.7 V) compared to the others ($U_{fb} = 1.03$ V and 0.93 V) and confirms also the effect of hydroxyls on the photoelectrochemical responses observed in Fig. 11b.

The photoelectrode stability was investigated for the three precursor combinations. Fig. 11c and d present the CV evolution for Alanis associated with O_3 and H_2O, respectively. Similar CVs for [Ni(^{i}pki)$_2$]/O_3 are shown in Fig. S17a, though no significant electrochemical changes were detected in this latter system. In the case of Alanis/O_3 (Fig. 11c), a minor j_{ph} decrease and a positive η shift are observed when comparing the initial and the 100th CVs. The anodic and cathodic waves associated with oxidation ($Ni^{2+} \rightarrow Ni^{3+} + e^-$) and reduction ($Ni^{3+} + e^- \rightarrow Ni^{2+}$) reactions, centred at 1 and 0.6 V, respectively, are considerably enhanced after 100 cycles. These electrochemical peaks usually reflect the Ni(OH)$_2$ and NiOOH phase

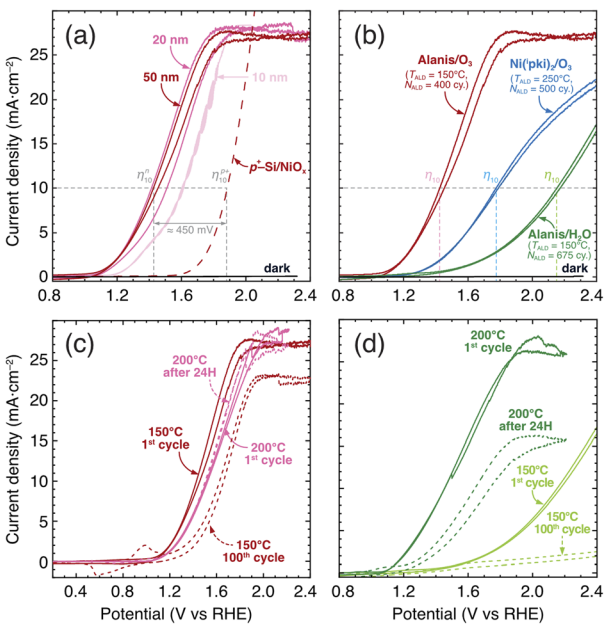

Fig. 11 CVs of NiO_x films deposited on Si performed in 1 M KOH in the dark and under illumination (AM1.5G). (a) NiO_x grown using Alanis/O_3 at 150 °C on n-Si exhibiting increasing thicknesses ($t_{NiO} = 10$, 20 and 50 nm) and on p$^+$-Si ($t_{NiO} = 50$ nm). (b) Initial CVs of the NiO_x grown using three precursor combinations (indicated on the plot). (c) Comparison of initial (full lines) CVs recorded on NiO_x deposited using Alanis/O_3 at 150 and 200 °C with CVs (dashed lines) after 100 cycles and after a CA experiment for 24 hours, respectively ($t_{NiO} = 50$ nm). (d) Comparison of initial CVs (full lines) recorded on NiO_x deposited using Alanis/H_2O at 150 and 200 °C with CVs (dashed lines) after 100 cycles and after a CA experiment for 24 hours, respectively ($t_{NiO} = 50$ nm).

Table 4 W_f and E_g of the NiO_x layers depending on the precursor combination

	Alanis/O_3	Alanis/H_2O	[Ni(^{i}pki)$_2$]/O_3
W_f (eV)	4.68	4.57	4.86
E_g (eV)	3.71	3.84	3.85

Open Access Article. Published on 04 November 2025. Downloaded on 1/29/2026 8:32:01 PM.
This article is licensed under a Creative Commons Attribution 3.0 Unported Licence.

transformations mentioned above. This is clearly visible in Fig. S17b where the progressive decrease of the current plateau correlates with the gradual enhancement of the peaks while cycling. This phenomenon is not observed when the films are grown with Alanis/O_3 at 200 °C. This might be ascribed to the lower $V_{Ni}^{\cdots}$ concentration (Table 3) that also leads to better stability.

In contrast, the Alanis/H_2O sample (Fig. 11d) exhibits a lower initial j_{ph} that further decreases significantly after 100 CV cycles. This reduced performance likely stems from elevated organic impurities in the film, which cause a tiny permeability and enable direct contact between the silicon substrate and electrolyte. The j_{ph} degradation may also be attributed to layer contamination, leading to subsequent delamination or dissolution of the films. A similar phenomenon has been reported for NiO_x grown by pulsed laser deposition.[24]

When depositions are carried out at $T_{ALD} = 200$ °C, the first CV for Alanis/O_3 remains almost unchanged, while it exhibits a significant enhancement of j_{ph} for Alanis/H_2O. The current plateau is then at the same level for both oxygen sources. After polarisation at $U = 2$ V under illumination for 24 hours, no change was observed for O_3, whereas the response for H_2O decreased by half. The consistent behaviour observed for O_3 is probably due to the negligible change in its properties, as suggested by the MS plot (Fig. 10d) and the better stability can arise from a higher density of the film shown by XRR measurements (Fig. 5). The j_{ph} enhancement of the film formed at $T_{ALD} = 200$ °C with H_2O probably comes from a higher density and lower impurity concentration.

The corresponding chronoamperograms (CAs) at $U = 2$ V under illumination are shown in Fig. 12a (the full timescale plot is shown in Fig. S18 for clarity). After an initial drop, the photocurrent remains stable for all three precursor combinations. Although the initial j_{ph} is lower for [Ni(^{i}pki)$_2$]/O_3, it shows a long-lasting stability (48 hours). In the case of Alanis/O_3, a stable j_{ph} is measured up to approximately 24 hours with almost no loss. As expected from the CVs of Alanis/H_2O, j_{ph} is reduced by half after 17 hours of polarisation. The stability is, however, significantly better at 200 °C (Fig. 11d). This can be attributed to their higher density and an O/Ni ratio that is closer to stoichiometry when the layers are produced at elevated temperatures. The degradation of NiO_x is further confirmed by XPS analysis performed after the electrochemical investigations. The delamination is indicated by the intense Si and SiO_x signals observed in the Si 2p XPS peak region (Fig. S19).

Given the different photoelectrochemical responses of the NiO_x layer, it is essential to investigate the possible chemical and crystalline modifications. Comparison of the XRD patterns collected before and after the electrochemical studies (Fig. 12b) shows the emergence of two new reflections at 33° and 59.4°, corresponding to the (101) and (300) planes of α-Ni(OH)$_2$, respectively (highlighted by * in the figure).[103,104] This confirms the phase transformations that occur during CVs. It should be noted that α-Ni(OH)$_2$ is detected *a posteriori* because it is the most stable phase. β-Ni(OH)$_2$ can be generated in solution but is unstable in air. *In situ* studies (XRD or XPS) are necessary to accurately identify it and clarify which compound induces the

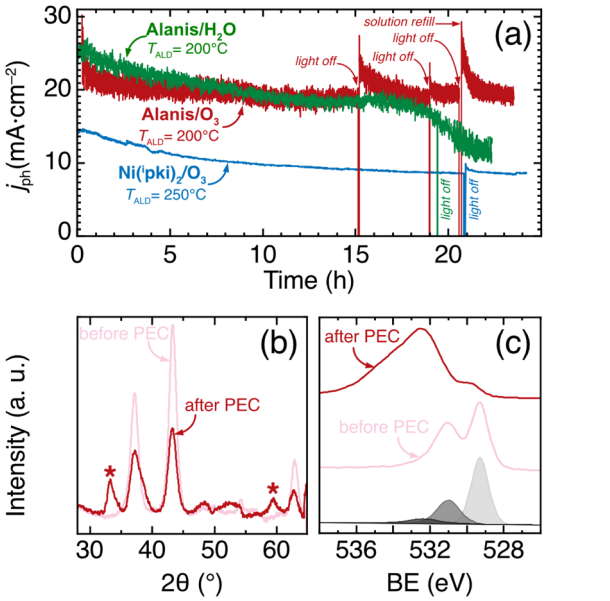

Fig. 12 (a) CAs at $U = 2$ V of NiO_x layers grown on n-Si under AM1.5G illumination for Alanis/O_3, Alanis/H_2O and [Ni(^{i}pki)$_2$]/O_3 combinations. T_{ALD} values are indicated on the plot. (b) XRD analysis of NiO_x before and after photoelectrochemical testing (Alanis/O_3 at 150 °C). The * signs are referenced in the text. (c) O 1s XPS peak of NiO_x before and after photoelectrochemical testing (Alanis/O_3 at 150 °C).

excellent catalytic activity. XPS analyses conducted before and after the PEC studies are consistent with CVs and XRD results. As shown in Fig. 12c, the O 1s peak shifts toward higher binding energies, corresponding to hydroxyl and water signatures. This indicates that the surface of the photoanode becomes hydroxylated, providing further evidence for the formation of Ni(OH)$_2$ or NiOOH.

4 Conclusion

In this study, NiO_x thin films were successfully deposited *via* thermal ALD using two novel precursors across three different precursor combinations. It demonstrates that combining the precursors with different co-reactants significantly influenced the film properties, including density, crystallinity, composition, surface roughness, and growth rate. Among them, the Alanis/O_3 combination exhibited the highest growth rate and a broad temperature window at relatively low deposition temperatures. It is one of the highest GPC values ever reported at $T_{ALD} \leq 200$ °C. Comprehensive structural, crystallographic, and morphological characterisation confirmed the formation of uniform, high-quality films with well-controlled growth behaviour. Optical and photoelectrochemical analyses further revealed that these films possess favorable properties for efficient water oxidation, demonstrating their potential in photoelectrochemical applications. These findings emphasise not only the viability of the new precursors for ALD but also the critical influence of precursor selection on the functional performance of NiO_x thin films. The present results are highly promising, as the onset potential for Alanis/O_3 is significantly

 This journal is © The Royal Society of Chemistry 2026

Open Access Article. Published on 04 November 2025. Downloaded on 1/29/2026 8:32:01 PM. This article is licensed under a Creative Commons Attribution 3.0 Unported Licence.

low ($U = 1.15$ V *vs.* RHE for $j_{ph} = 1$ mA cm^{-2}), ranking among the best reported in the literature (see the benchmark in Fig. S20). Moreover, optimisation of the ALD process has resulted in 50 nm-thick films exhibiting long-lasting stability when other methods, such as PLD, require almost twice the thickness to be comparable.[24] These electrochemical performances seem to be correlated with the high O concentration and, more particularly, with OH at the surface of the film. Future work will focus on further optimising deposition parameters (*e.g.* post-deposition thermal treatments) and applying such processes to micro- or nano-structured Si to further improve the OER and assess the practical applicability of n-Si/NiO_x in solar-driven water splitting technologies.

Author contributions

V. Kannampalli: writing – original draft, validation, methodology, investigation (fabrication and characterisation of the photoelectrodes), formal analysis, data curation, and conceptualisation. M. Schmickler: writing – review & editing, validation, investigation (synthesis and characterisation) and formal analysis. B. Fabre: writing review & editing, validation, and investigation (characterisation). L. Largeau: writing review & editing, validation, and investigation (characterisation). A. Seyeux: writing review & editing, validation, and investigation (characterisation). J. Alvarez: writing review & editing, validation, and investigation (characterisation). S. D. Elliott: writing – original draft, validation, and investigation (mechanisms). A. Devi: writing – review & editing, validation, methodology, investigation (synthesis and characterisation), supervision, resources, and formal analysis. L. Santinacci: writing – original draft, validation, investigation, supervision, resources, project administration, formal analysis, data curation, and conceptualisation.

Conflicts of interest

There are no conflicts to declare.

Data availability

The data supporting this article have been included as part of the supplementary information (SI). Supplementary information is available. See DOI: **https://doi.org/10.1039/d5ta04555j**.

Acknowledgements

Vasile Heresanu (CINaM-CNRS) is acknowledged for his precious help with XRD analyses. Dr Corinne Lagrost from the ASPHERYX platform (CNRS – University of Rennes) is also acknowledged for XPS measurements. Nicolas Blasco and Jamie Greer from Air Liquide Advanced Materials are acknowledged for providing the Ni precursor. This collaborative work was supported by the French Agence Nationale de la Recherche (ANR) under grant ANR-23-CE50-0024-01 (EffiCaWat project) and by the France 2030 PEPR H_2 program managed by the ANR under the grant ANR-22-PEHY-0013 (Nautilus project). V. K. acknowledges the Council of Région Sud for funding (DEB #DEP 21-387, 23/07/2021). A. D. and M. S. acknowledge the DFG for supporting this work (REACTIVE project, No. 490773082). This work was partly supported by the French Renatech network (FIB preparation, TEM observations).

References

1 K. Nomura, H. Ohta, A. Takagi, T. Kamiya, M. Hirano and H. Hosono, *Nature*, 2004, **432**, 488–492.
2 J. W. Park, B. H. Kang and H. J. Kim, *Adv. Funct. Mater.*, 2020, **30**, 1904632.
3 M. Coll, J. Fontcuberta, M. Althammer, M. Bibes, H. Boschker and A. Calleja, *Appl. Surf. Sci.*, 2019, **482**, 1–93.
4 R. L. Z. Hoye, K. P. Musselman and J. L. MacManus-Driscoll, *APL Mater.*, 2013, **1**, 060701.
5 L. Petti, N. Münzenrieder, C. Vogt, H. Faber, L. Büthe, G. Cantarella, F. Bottacchi, T. D. Anthopoulos and G. Tröster, *Appl. Phys. Rev.*, 2016, **3**, 021303.
6 M. Napari, T. N. Huq, R. L. Z. Hoye and J. L. MacManus-Driscoll, *InfoMat*, 2021, **3**, 536–576.
7 E. M. C. Fortunato, P. M. C. Barquinha, A. C. M. B. G. Pimentel, A. M. F. Gonçalves, A. J. S. Marques, L. M. N. Pereira and R. F. P. Martins, *Adv. Mater.*, 2005, **17**, 590–594.
8 S. K. Garlapati, J. S. Gebauer, S. Dehm, M. Bruns, M. Winterer, H. Hahn and S. Dasgupta, *Adv. Electron. Mater.*, 2017, **3**, 1600476.
9 M. D. Irwin, J. D. Servaites, D. B. Buchholz, B. J. Leever, J. Liu, J. D. Emery, M. Zhang, J.-H. Song, M. F. Durstock, A. J. Freeman, M. J. Bedzyk, M. C. Hersam, R. P. H. Chang, M. A. Ratner and T. J. Marks, *Chem. Mater.*, 2011, **23**, 2218–2226.
10 H.-J. Kim and J.-H. Lee, *Sens. Actuators, B*, 2014, **192**, 607–627.
11 K. Nomura, T. Kamiya and H. Hosono, *Adv. Mater.*, 2011, **23**, 3431–3434.
12 Z. Wang, P. K. Nayak, J. A. Caraveo-Frescas and H. N. Alshareef, *Adv. Mater.*, 2016, **28**, 3831–3892.
13 T. S. Tripathi and M. Karppinen, *Adv. Mater. Interfaces*, 2017, **4**, 1700300.
14 J. Zhang, D. Zeng, Q. Zhu, J. Wu, Q. Huang and C. Xie, *J. Phys. Chem. C*, 2016, **120**, 3936–3945.
15 J. Wang, K. Liu, W. Liao, Y. Kang, H. Xiao, Y. Chen, Q. Wang, T. Luo, J. Chen, H. Li, *et al.*, *Nat. Catal.*, 2025, 1–10.
16 F. Jiang, W. C. Choy, X. Li, D. Zhang and J. Cheng, *Adv. Mater.*, 2015, **27**, 2930–2937.
17 S. Lany, J. Osorio-Guillén and A. Zunger, *Phys. Rev. B*, 2007, **75**, 241203.
18 J. Zhang, D. Zeng, Q. Zhu, J. Wu, K. Xu, T. Liao, G. Zhang and C. Xie, *J. Phys. Chem. C*, 2015, **119**, 17930–17939.
19 D.-Y. Cho, S. J. Song, U. K. Kim, K. M. Kim, H.-K. Lee and C. S. Hwang, *J. Mater. Chem. C*, 2013, **1**, 4334.
20 H. Radinger, P. Connor, S. Tengeler, R. W. Stark, W. Jaegermann and B. Kaiser, *Chem. Mater.*, 2021, **33**, 8259–8266.

Open Access Article. Published on 04 November 2025. Downloaded on 1/29/2026 8:32:01 PM. This article is licensed under a Creative Commons Attribution 3.0 Unported Licence.

21 N. Weidler, J. Schuch, F. Knaus, P. Stenner, S. Hoch, A. Maljusch, R. Schäfer, B. Kaiser and W. Jaegermann, *J. Phys. Chem. C*, 2017, **121**, 6455–6463.
22 G. Boschloo and A. Hagfeldt, *J. Phys. Chem. B*, 2001, **105**, 3039–3044.
23 K. Sun, F. H. Saadi, M. F. Lichterman, W. G. Hale, H.-P. Wang, X. Zhou, N. T. Plymale, S. T. Omelchenko, J.-H. He, K. M. Papadantonakis, B. S. Brunschwig and N. S. Lewis, *Proc. Natl. Acad. Sci. U. S. A.*, 2015, **112**, 3612–3617.
24 L. He, W. Zhou, D. Cai, S. S. Mao, K. Sun and S. Shen, *Catal. Sci. Technol.*, 2017, **7**, 2632–2638.
25 S. Tengeler, M. Fingerle, W. Calvet, C. Steinert, B. Kaiser, T. Mayer and W. Jaegermann, *J. Electrochem. Soc.*, 2018, **165**, H3122.
26 S. Hu, M. R. Shaner, J. A. Beardslee, M. Lichterman, B. S. Brunschwig and N. S. Lewis, *Science*, 2014, **344**, 1005–1009.
27 P. Misra, V. K. Sahu, R. S. Ajimsha, A. K. Das and B. Singh, *J. Phys. D: Appl. Phys.*, 2017, **50**, 415106.
28 P. Salunkhe, A. A. V. Muhammed and D. Kekuda, *Appl. Phys. A*, 2021, **127**, 390.
29 S. Pereira, A. Gonçalves, N. Correia, J. Pinto, L. Pereira, R. Martins and E. Fortunato, *Sol. Energy Mater. Sol. Cells*, 2014, **120**, 109–115.
30 D. Mateos, B. Valdez, J. Castillo, N. Nedev, M. Curiel, O. Perez, A. Arias and H. Tiznado, *Ceram. Int.*, 2019, **45**, 11403–11407.
31 T. Ivanova, A. Harizanova, M. Shipochka and P. Vitanov, *Materials*, 2022, **15**, 1742.
32 T. M. Roffi, S. Nozaki and K. Uchida, *J. Cryst. Growth*, 2016, **451**, 57–64.
33 M. Aftab, M. Butt, D. Ali, F. Bashir and T. M. Khan, *Opt. Mater.*, 2021, **119**, 111369.
34 H. Kumagai, M. Matsumoto, K. Toyoda and M. Obara, *J. Mater. Sci. Lett.*, 1996, **15**, 1081–1083.
35 H. L. Lu, G. Scarel, C. Wiemer, M. Perego, S. Spiga, M. Fanciulli and G. Pavia, *J. Electrochem. Soc.*, 2008, **155**, H807.
36 D. Koushik, M. Jošt, A. Dučinskas, C. Burgess, V. Zardetto, C. Weijtens, M. A. Verheijen, W. M. M. Kessels, S. Albrecht and M. Creatore, *J. Mater. Chem. C*, 2019, **7**, 12532–12543.
37 V. Zardetto, B. L. Williams, A. Perrotta, F. Di Giacomo, M. A. Verheijen, R. Andriessen, W. M. M. Kessels and M. Creatore, *Sustain. Energy Fuels*, 2017, **1**, 30–55.
38 L. Santinacci, M. W. Diouf, M. K. S. Barr, B. Fabre, L. Joanny, F. Gouttefangeas and G. Loget, *ACS Appl. Mater. Interfaces*, 2016, **8**, 24810–24818.
39 H. B. Profijt, S. E. Potts, M. C. M. Van De Sanden and W. M. M. Kessels, *J. Vac. Sci. Technol., A*, 2011, **29**, 050801.
40 D. Garcia-Alonso, S. E. Potts, C. A. A. Van Helvoirt, M. A. Verheijen and W. M. M. Kessels, *J. Mater. Chem. C*, 2015, **3**, 3095–3107.
41 M. E. Dufond, M. W. Diouf, C. Badie, C. Laffon, P. Parent, D. Ferry, D. Grosso, J. C. S. Kools, S. D. Elliott and L. Santinacci, *Chem. Mater.*, 2020, **32**, 1393–1407.
42 M. E. Dufond, J.-N. Chazalviel and L. Santinacci, *J. Electrochem. Soc.*, 2021, **168**, 031509.
43 S. Haghverdi Khamene, C. Van Helvoirt, M. N. Tsampas and M. Creatore, *J. Phys. Chem. C*, 2023, **127**, 22570–22582.
44 J. Chae, H.-S. Park and S.-w. Kang, *Electrochem. Solid-State Lett.*, 2002, **5**, C64.
45 J. Bachmann, A. Zolotaryov, O. Albrecht, S. Goetze, A. Berger, D. Hesse, D. Novikov and K. Nielsch, *Chem. Vap. Depos.*, 2011, **17**, 177–180.
46 L. Assaud, E. Monyoncho, K. Pitzschel, A. Allagui, M. Petit, M. Hanbücken, E. A. Baranova and L. Santinacci, *Beilstein J. Nanotechnol.*, 2014, **5**, 162–172.
47 H. Lu, G. Scarel, X. Li and M. Fanciulli, *J. Cryst. Growth*, 2008, **310**, 5464–5468.
48 T. S. Yang, W. Cho, M. Kim, K.-S. An, T.-M. Chung, C. G. Kim and Y. Kim, *J. Vac. Sci. Technol., A*, 2005, **23**, 1238–1243.
49 P. Antony Premkumar, M. Toeller, C. Adelmann, J. Meersschaut, A. Franquet, O. Richard, H. Tielens, B. Brijs, A. Moussa, T. Conard, H. Bender, M. Schaekers, J. A. Kittl, M. Jurczak and S. Van Elshocht, *Chem. Vap. Depos.*, 2012, **18**, 61–69.
50 U. Farva and J. Kim, *Vacuum*, 2023, **207**, 111674.
51 R. Attri, D. P. Panda, J. Ghatak and C. N. R. Rao, *APL Mater.*, 2023, **11**, 091105.
52 M. Utriainen, M. Kröger-Laukkanen and L. Niinistö, *Mater. Sci. Eng., B*, 1998, **54**, 98–103.
53 E. Thimsen, A. B. F. Martinson, J. W. Elam and M. J. Pellin, *J. Phys. Chem. C*, 2012, **116**, 16830–16840.
54 Y. Zhang, L. Du, X. Liu and Y. Ding, *Appl. Surf. Sci.*, 2019, **481**, 138–143.
55 M. Ritala and M. Leskelä, in *Handbook of Thin Films*, Elsevier, 2002, pp. 103–159.
56 M. Leskelä and M. Ritala, *Angew. Chem., Int. Ed.*, 2003, **42**, 5548–5554.
57 T. Blanquart, J. Niinistö, M. Ritala and M. Leskelä, *Chem. Vap. Depos.*, 2014, **20**, 189–208.
58 J. P. Klesko, M. M. Kerrigan and C. H. Winter, *Chem. Mater.*, 2016, **28**, 700–703.
59 K. E. K. Holden, C. L. Dezelah and J. F. Conley, *ACS Appl. Mater. Interfaces*, 2019, **11**, 30437–30445.
60 M.-H. Ko, B. Shong and J.-H. Hwang, *Ceram. Int.*, 2018, **44**, 16342–16351.
61 V. Pore, E. Tois, R. Matero, S. Haukka, M. Tuominen, J. Woodruff, B. Milligan, F. Tang and M. Givens, in *2015 IEEE International Interconnect Technology Conference and 2015 IEEE Materials for Advanced Metallization Conference (IITC/MAM)*, Grenoble, 2015, pp. 191–194.
62 D. Zywitzki, D. H. Taffa, L. Lamkowski, M. Winter, D. Rogalla, M. Wark and A. Devi, *Inorg. Chem.*, 2020, **59**, 10059–10070.
63 S. Porcar, M. Schmickler, H. Okcu, J. Obenlüneschloß, S. d'Ercole, L. Cervera-Gabalda, I. Galarreta-Rodriguez, J. Rubio-Zuazo, J. G. Cuadra, A. Lahlahi, D. Fraga, C. Sanchez-Velasquez, D. Bellet, T. Fix, J. B. Carda, A. Devi and D. Muñoz-Rojas, *Appl. Surf. Sci. Adv.*, 2025, **29**, 100836.

 This journal is © The Royal Society of Chemistry 2026

Open Access Article. Published on 04 November 2025. Downloaded on 1/29/2026 8:32:01 PM. This article is licensed under a Creative Commons Attribution 3.0 Unported Licence.

64 D. Peeters, A. Sadlo, K. Lowjaga, O. Mendoza Reyes, L. Wang, L. Mai, M. Gebhard, D. Rogalla, H. Becker, I. Giner, G. Grundmeier, D. Mitoraj, M. Grafen, A. Ostendorf, R. Beranek and A. Devi, *Adv. Mater. Interfaces*, 2017, **4**, 1700155.
65 M. K. Barr, L. Assaud, Y. Wu, C. Laffon, P. Parent, J. Bachmann and L. Santinacci, *Electrochim. Acta*, 2015, **179**, 504–511.
66 T. Peng, X. Xiao, X. Han, X. Zhou, W. Wu, F. Ren and C. Jiang, *Appl. Surf. Sci.*, 2011, **257**, 5908–5912.
67 Available on request from Air Liquide Advanced Materials 3040 US-22, Branchburg, NJ 08876, USA, gregory.muhr@airliquide.com, usalam-orders@airliquide.com, Liquide, Air.
68 C. Badie, A. Mirzaei, J. Lee, S. Sayegh, M. Bechelany, L. Santinacci, H. W. Kim and S. S. Kim, *Adv. Mater. Technol.*, 2024, **9**, 2302081.
69 C.-C. Hsu, H.-W. Su, C.-H. Hou, J.-J. Shyue and F.-Y. Tsai, *Nanotechnology*, 2015, **26**, 385201.
70 D. N. Goldstein and S. M. George, *Thin Solid Films*, 2011, **519**, 5339–5347.
71 R. Zhao, S. Xiao, S. Yang and X. Wang, *Chem. Mater.*, 2019, **31**, 5172–5180.
72 C. Ehinger, X. Zhou, M. Candrian, S. R. Docherty, S. Pollitt and C. Copéret, *JACS Au*, 2023, **3**, 2314–2322.
73 X. Zhang, Z. Zhou, R. Xu, J. Guo, L. Xu, Y. Ding, H. Xiao, X. Li, A. Li and G. Fang, *Phys. Chem. Chem. Phys.*, 2023, **25**, 13465–13473.
74 D. Franta, B. Negulescu, L. Thomas, P. R. Dahoo, M. Guyot, I. Ohlídal, J. Mistrík and T. Yamaguchi, *Appl. Surf. Sci.*, 2005, **244**, 426–430.
75 J. W. F. Innocent, M. Napari, A. L. Johnson, T. R. Harris-Lee, M. Regue, T. Sajavaara, J. L. MacManus-Driscoll, F. Marken and F. Alkhalil, *Mater. Adv.*, 2021, **2**, 273–279.
76 R. J. Powell and W. E. Spicer, *Phys. Rev. B*, 1970, **2**, 2182–2193.
77 H. L. Lu, G. Scarel, M. Alia, M. Fanciulli, S.-J. Ding and D. W. Zhang, *Appl. Phys. Lett.*, 2008, **92**, 222907.
78 A. López-Beltrán and A. Mendoza-Galván, *Thin Solid Films*, 2006, **503**, 40–44.
79 L. Santinacci, M. Bouttemy, M. Petit, A.-M. Gonçalves, N. Simon, J. Vigneron and A. Etcheberry, *J. Electrochem. Soc.*, 2018, **165**, H3131.
80 A. P. Grosvenor, M. C. Biesinger, R. S. Smart and N. S. McIntyre, *Surf. Sci.*, 2006, **600**, 1771–1779.
81 M. A. Peck and M. A. Langell, *Chem. Mater.*, 2012, **24**, 4483–4490.
82 D. Wanger, W. M. Riggs, L. E. Davis, J. F. Moulder and G. E. Muilenberg, in *Handbook of X-Ray Photoelectron Spectroscopy*, Perkin-Elmer Corp., Physical Electronics Division, Eden Prairie, Minnesota, USA, 1979.
83 M. A. Van Veenendaal and G. A. Sawatzky, *Phys. Rev. Lett.*, 1993, **70**, 2459–2462.
84 S. Chakrabarti, D. Carolan, B. Alessi, P. Maguire, V. Svrcek and D. Mariotti, *Nanoscale Adv*, 2019, **1**, 4915–4925.
85 S. Timoshnev, A. Kazakin, K. Shubina, V. Andreeva, E. Fedorenko, A. Koroleva, E. Zhizhin, O. Koval, A. Kurinnaya, A. Shalin, V. Bobrovs and Y. Enns, *Adv. Mater. Interfaces*, 2024, **11**, 2300815.
86 K. S. Usha, R. Sivakumar, C. Sanjeeviraja, V. Sathe, V. Ganesan and T. Y. Wang, *RSC Adv.*, 2016, **6**, 79668–79680.
87 A. N. Mansour and C. A. Melendres, *Surf. Sci. Spectra*, 1994, **3**, 263–270.
88 A. N. Mansour, *Surf. Sci. Spectra*, 1994, **3**, 239–246.
89 P. Nandi, H. Park, S. Shin, J. Lee, J. Y. Kim, M. J. Ko, H. S. Jung, N. Park and H. Shin, *Adv. Mater. Interfaces*, 2024, **11**, 2300751.
90 Y. S. Chen, J. F. Kang, B. Chen, B. Gao, L. F. Liu, X. Y. Liu, Y. Y. Wang, L. Wu, H. Y. Yu, J. Y. Wang, Q. Chen and E. G. Wang, *J. Phys. D: Appl. Phys.*, 2012, **45**, 065303.
91 H. Park, P. Nandi, Y. In and H. Shin, *Sol. RRL*, 2024, **8**, 2300858.
92 B. Zhao, L. C. Lee, L. Yang, A. J. Pearson, H. Lu, X.-J. She, L. Cui, K. H. Zhang, R. L. Hoye, A. Karani, *et al.*, *ACS Appl. Mater. Interfaces*, 2018, **10**, 41849–41854.
93 G. A. Sawatzky and J. W. Allen, *Phys. Rev. Lett.*, 1984, **53**, 2339–2342.
94 S. Battiato, M. M. Giangregorio, M. R. Catalano, R. Lo Nigro, M. Losurdo and G. Malandrino, *RSC Adv.*, 2016, **6**, 30813–30823.
95 R. Poulain, G. Lumbeeck, J. Hunka, J. Proost, H. Savolainen, H. Idrissi, D. Schryvers, N. Gauquelin and A. Klein, *ACS Appl. Electron. Mater.*, 2022, **4**, 2718–2728.
96 J. Keraudy, B. Delfour-Peyrethon, A. Ferrec, J. Garcia Molleja, M. Richard-Plouet, C. Payen, J. Hamon, B. Corraze, A. Goullet and P.-Y. Jouan, *J. Appl. Phys.*, 2017, **121**, 171916.
97 S.-H. Lee, H. M. Cheong, N.-G. Park, C. Tracy, A. Mascarenhas, D. K. Benson and S. K. Deb, *Solid State Ionics*, 2001, **140**, 135–139.
98 R. Newman and R. M. Chrenko, *Phys. Rev.*, 1959, **114**, 1507–1513.
99 S. Seo, I. J. Park, M. Kim, S. Lee, C. Bae, H. S. Jung, N.-G. Park, J. Y. Kim and H. Shin, *Nanoscale*, 2016, **8**, 11403–11412.
100 H. L. S. Santos, P. G. Corradini, M. A. S. Andrade and L. H. Mascaro, *J. Solid State Electrochem.*, 2020, **24**, 1899–1908.
101 Q. Liu, L. Wei, S. Yuan, X. Ren, Y. Zhao, Z. Wang, M. Zhang, L. Shi, D. Li and A. Li, *RSC Adv.*, 2015, **5**, 71778–71784.
102 Y. Yu, K. A. Click, S.-C. Chien, J. Sun, A. Curtze, L.-C. Lin and Y. Wu, *J. Phys. Chem. C*, 2019, **123**, 8681–8687.
103 S. Zhou, W. Wei, Y. Zhang, S. Cui, W. Chen and L. Mi, *Sci. Rep.*, 2019, **9**, 12727.
104 J. Deng, M. R. Nellist, M. B. Stevens, C. Dette, Y. Wang and S. W. Boettcher, *Nano Lett.*, 2017, **17**, 6922–6926.